

GROWTH AND CHARACTERIZATION
OF INDIUM RICH INDIUM-GALLIUM-NITRIDE SOLAR CELL
EPITAXIAL STRUCTURES BY METAL ORGANIC CHEMICAL VAPOR
DEPOSITION

A THESIS SUBMITTED TO
THE GRADUATE SCHOOL OF NATURAL AND APPLIED SCIENCE
OF
MIDDLE EAST TECHNICAL UNIVERSITY

BY

HÜSEYİN ÇAKMAK

IN PARTIAL FULFILLMENT OF THE REQUIREMENTS
FOR
THE DEGREE OF MASTER OF SCIENCE
IN
MICRO AND NANOTECHNOLOGY

DECEMBER 2012

Approval of the thesis:

**THE GROWTH AND CHARACTERIZATION
OF INDIUM RICH INDIUM-GALLIUM-NITRIDE (INGAN) SOLAR
CELL EPITAXIAL STRUCTURES BY METAL ORGANIC CHEMICAL
VAPOR DEPOSITION (MOCVD)**

submitted by **HÜSEYİN ÇAKMAK** in partial fulfillment of the requirements for
the degree of **Master of Science in Micro and Nanotechnology Department,**
Middle East Technical University by,

Prof. Dr. Canan Özgen
Dean, Graduate School of **Natural and Applied Sciences** _____

Prof. Dr. Mürvet Volkan
Head of Department, **Micro and Nanotechnology** _____

Assoc. Prof. Dr. Hüsnü Emrah Ünalın
Supervisor, **Metallurgical and Materials Dept., METU** _____

Prof. Dr. Raşit Turan
Co-Supervisor, **Physics Dept., METU** _____

Examining Committee Members:

Prof. Dr. Tayfur Öztürk
Metallurgical and Materials Dept., METU _____

Assoc. Prof. Dr. Hüsnü Emrah Ünalın
Metallurgical and Materials Dept., METU _____

Prof. Dr. Raşit Turan
Physics Dept., METU _____

Prof. Dr. Ekmel Özbay
Physics Dept., Bilkent University _____

Assist. Prof. Dr. Alpan Bek
Physics Dept., METU _____

Date: _____

I hereby declare that all information in this document has been obtained and presented in accordance with academic rules and ethical conduct. I also declare that, as required by these rules and conduct, I have fully cited and referenced all material and results that are not original to this work.

Name, Last Name: Huseyin ÇAKMAK

Signature:

ABSTRACT

GROWTH AND CHARACTERIZATION OF INDIUM RICH INDIUM-GALLIUM-NITRIDE SOLAR CELL EPITAXIAL STRUCTURES BY METAL ORGANIC CHEMICAL VAPOR DEPOSITION

Çakmak, Hüseyin

M. Sc., Department of Micro and Nanotechnology

Supervisor : Assist. Prof. Dr. Hüsnü Emrah Ünalın

Co-Supervisor : Prof. Dr. Raşit Turan

December 2012, 79 pages

The purpose of this study is to develop a technology for indium (In) rich indium gallium nitride (InGaN) solar cell epitaxial structures through metal organic chemical vapor deposition (MOCVD) method. $\text{In}_x\text{Ga}_{1-x}\text{N}$ solar cell structures have potential to cover 90% of the solar spectrum by varying In composition in the active region of the solar cell, where bandgaps of indium nitride (InN) and gallium nitride (GaN) are 0.7 eV and 3.4 eV, respectively. Photovoltaic devices that have a bandgap larger than 2.0 eV gather great interest since half of the available photons in the solar spectrum belongs there. However, only limited success has been achieved to increase the amount of In incorporation into InGaN epitaxial structures.

This thesis is focused on the epitaxial growth of In rich InGaN epitaxial structures. These InGaN structures were grown on double side polished (DSP) c-plane sapphire substrates using MOCVD and then utilized for solar cells. Solar cell device characterizations were carried out after standart microfabrication procedures. X-Ray diffraction (XRD), Hall-Effect Measurements and absorption measurements have been done to investigate material properties first. Afterwards

then the current voltage (I-V) characterizations were performed to investigate solar cell device performance.

XRD measurements revealed that both GaN and InGaN epitaxial structures have high crystal quality, where full width at half maximum (FWHM) values of around 300 arcsec and 400 arcsec for GaN and InGaN epilayers were obtained, respectively. In content was found to increase light absorption. Highest photovoltaic conversion of 0.66% was achieved for In_{0.16}GaN films under a standard solar simulator with one-sun air mass (AM) 1.5 global light source (100mW/cm²) at room temperature. The solar simulator was calibrated with a standard solar cell before measurements.

There is a increase on light absorption with increasing indium content in epitaxial structures. The best efficiency that was reached is 0.66% under air mass (AM) 1.5 global light source.

Keywords: In rich InGaN, solar cell MOCVD, epitaxial growth

ÖZ

INDIUM ORANI YÜKSEK INDIUM GALYUM NİTRAT GÜNEŞ PİLİ EPİTAKSİYEL YAPILARININ METAL ORGANİK KİMYASAL BUHAR BİRİKTİRME YÖNTEMİ İLE BÜYÜTÜLMESİ VE KARAKTERİZASYONU

Çakmak, Hüseyin

Yüksek Lisans, Mikro ve Nanoteknoloji Bölümü

Tez Yöneticisi : Yrd. Doç. Dr. Hüsnü Emrah Ünalın

Ortak Tez Yöneticisi : Prof. Dr. Raşit Turan

Aralık 2012, 79 sayfa

Bu çalışmanın amacı Metal Organik Kimyasal Buhar Biriktirme Sistemiyle (MOCVD) Indiyum (In) zengini Indiyum Galyum Nitrat (InGaN) güneş pili epitaksiyel yapıları için teknoloji geliştirmektir. Indiyum Nitrat (InN) ve Galyum Nitrat (GaN) malzemelerinin yasak bant aralıklarının 0.7 eV ve 3.4 eV olduğu göz önünde bulundurulursa, $In_xGa_{1-x}N$ güneş pili yapıları, In konsantrasyonunun değişimine bağlı olarak güneş spektrumunun %90'lık bir kısmını kapsama özelliğine sahiptir. Güneş spektrumundaki uygun fotonların yarısı bu aralıkta bulunduğundan yasak bant aralığı 2 eV dan fazla olan fotovoltaik aygıtlar büyük ilgi toplamaktadır. Buna rağmen, InGaN epitaksiyel yapılarındaki In oranını arttırmak için sınırlı sayıda başarı elde edilmiştir.

Bu tez In zengini InGaN epitaksiyel yapıları ile ilgilidir. Bu InGaN yapıları çift tarafı parlatılmış (DSP) safir alttaşların c-düzlemi üzerine MOCVD sistemi ile büyütülmüştür ve sonrasında güneş pili yapılarında kullanılmıştır. Güneş pili aygıt karakterizasyonu standart mikrofabrikasyon prosedüründen sonra yapılmıştır. Malzeme özelliklerinin analizi için ilk önce X ışını difraktometresi (XRD), Hall etkisi ve absorpsiyon ölçümleri gerçekleştirilmiştir. Ayrıca aygıt performansı değerlendirmesi için akım voltaj (I-V) karakterizasyonu yapılmıştır.

X ışını karakterizasyonları hem GaN hem InGaN epitaksiyel yapılarının yüksek kristal kalitesine sahip olduğunu göstermiştir. Yarı yükseklikte tam genişlik (FWHM) değerleri GaN tabakaları için 300 arcsec civarında, InGaN tabakaları için 400 arcsec'dan azdır.

Epitaksiyel yapılarda In konsantrasyonu arttıkça ışık absorpsiyonunda da artış görülmüştür. En yüksek verimlilik değeri AM1.5G ışık kaynağı altında $\text{In}_{0,16}\text{GaN}$ yapılarda %0.66 elde edilmiştir.

Anahtar Kelimeler: In oranı yüksek InGaN, güneş pili, MOCVD, epitaksiyel büyütme

To my daughter, Eylül

ACKNOWLEDGMENTS

I would like to express my thanks to my supervisor Assoc. Prof. Dr. Hüsnu Emrah Ünalan for his guidance, motivation and support. I would like to thank to my co-adviser Prof. Dr. Raşit Turan for his valuable guidance during my master's period.

I hereby present my sincere gratitude to Prof. Dr. Ekmel Ozbay for providing excellent working conditions and encouragement.

I would like to thank my committee members Prof. Dr. Raşit Turan, Prof. Dr. Ekmel Özbay, Prof. Dr. Tayfur Öztürk, Assoc. Prof. Dr. Hüsnu Emrah Ünalan and Assist. Prof. Dr. Alpan Bek for their time and helpful comments.

I would like to thank my former and present colleague Mustafa Öztürk, Yasemin Kanlı, Pakize Demirel and Ayça Emen. My special thanks go to my office colleague Assist. Prof. Dr. Engin Arslan for his endless help and encouragement.

Finally, I am indebted to my lovely wife for her continuous support and care.

TABLE OF CONTENTS

| | |
|--------------------------------------------------------|------|
| Abstract | iv |
| Öz..... | vi |
| Acknowledgements | ix |
| Table of Contents | x |
| List of Tables..... | xii |
| List of Figures..... | xiii |
| Chapters | |
| 1. Introduction | 1 |
| 1.1. Properties of III-Nitrides. | 5 |
| 1.2. Application of III-Nitrides | 7 |
| 1.3. Substrates | 7 |
| 1.4. Growth Techniques | 8 |
| 2. Metal-Organic Chemical Vapor Deposition Method..... | 10 |
| 2.1. Epitaxy | 10 |
| 2.2. MOCVD Growth Technique | 11 |
| 2.2.1. Configuration | 12 |
| 2.2.2. Sources | 14 |
| 3. Solar Cell Design | 17 |
| 3.1. Conversion of Solar Energy | 17 |
| 3.2. Band Diagram of a Solar Cell | 18 |
| 3.3. Solar Cell Structure | 20 |
| 3.3.1. Single Junction Solar Cells | 22 |
| 3.3.2. Tandem Solar Cells for High Efficiency | 22 |
| 3.3.3. The InGaN Material System | 25 |
| 4. Characterization Techniques | 28 |

| | | |
|--------|---------------------------------------------------------|----|
| 4.1. | In-situ Characterization | 28 |
| 4.2. | X-ray Diffraction | 31 |
| 4.3. | Atomic Force Microscopy (AFM) | 33 |
| 4.4. | Hall Effects Measurement | 33 |
| 4.5. | Absorption Measurements..... | 35 |
| 4.6. | Solar Cell Characterization | 36 |
| 5. | Experimental Details | 40 |
| 5.1. | In rich InGaN Thin Film Growth by MOCVD | 40 |
| 5.2. | InGaN Solar Cell Design | 42 |
| 5.2.1. | Band Simulations for InGaN Solar Cell | 42 |
| 5.2.2. | Preliminary Growth | 44 |
| 5.2.3. | InGaN Solar Cell Growth | 45 |
| 5.3. | Fabrication of Solar Cell..... | 47 |
| 6. | Results and Discussion | 50 |
| 6.1. | Characterization of In rich InGaN Epilayers | 50 |
| 6.1.1. | In-situ Characterization | 50 |
| 6.1.2. | XRD Measurements | 52 |
| 6.1.3. | Atomic Force Microscopy (AFM) Measurements... 55 | |
| 6.1.4. | Hall Effect Measurements | 56 |
| 6.1.5. | Absorption Measurements | 58 |
| 6.2. | InGaN Solar Cell Characterization | 61 |
| 6.2.1. | Material Characterization for Solar Cell Structure.. 61 | |
| 6.2.2. | Absorption Measurement of Solar Cell Structures.. 64 | |
| 6.2.3. | Current Density Voltage (I-V) Characteristics | 66 |
| 7. | Conclusions | 71 |
| 8. | Future Directions | 73 |
| | List of References | 74 |

LIST OF TABLES

TABLES

| | |
|---------------------------------------------------------------------------------------------------------------------------|----|
| Table 1.1. Properties of group III-nitrides | 6 |
| Table 2.1. Sources of MOCVD system | 15 |
| Table 3.1. Theoretical efficiency calculation for a tandem solar cell that have different band gap materials | 26 |
| Table 6.1. Characterization measurements of epilayers and literature comparison | 63 |
| Table 6.2. Solar Cell parameters | 68 |

LIST OF FIGURES

FIGURES

| | |
|---------------------------------------------------------------------------------------------|----|
| Figure 1.1. Global carbon dioxide emissions from fossil fuels | 2 |
| Figure 1.2. Consumption of various resources and corresponding oil consumption | 3 |
| Figure 1.3. Best research cell efficiencies | 4 |
| Figure 1.4. Crystal constant and band gap for various semiconducting materials..... | 8 |
| Figure 2.1. Schematic steps for MOCVD growth | 12 |
| Figure 2.2. Simple diagram of a MOCVD system | 13 |
| Figure 2.3. Simple diagram of MOCVD reactor | 14 |
| Figure 3.1. Solar spectrums | 18 |
| Figure 3.2. Energy band structure of a n and p-type doped semiconductor | 19 |
| Figure 3.3. Energy band structures of the p-n heterojunctions | 19 |
| Figure 3.4. Basic operation principle of a solar cell | 20 |
| Figure 3.5. Cross section of a solar cell | 21 |

| | |
|------------------------------------------------------------------------------------------------------------------------------------------|----|
| Figure 3.6. Tandem solar cell concepts | 22 |
| Figure 3.7. AM1.5 spectrum and parts of the spectrum that can be used by a) Si solar cell and b) triple-junction solar cell | 23 |
| Figure 3.8. Multi junction solar cell structure and covered solar spectrum | 24 |
| Figure 3.9. Band gaps of the materials as a function of lattice constant | 25 |
| Figure 3.10. Solar spectrum for III-V solar cells | 27 |
| Figure 4.1. Schematic for in-situ reflectance measurement setup | 29 |
| Figure 4.2. Reflection of light from surfaces | 29 |
| Figure 4.3. Reflectance of a) ideal growth, b) increasing material thickness and c) increasing surface roughness | 30 |
| Figure 4.4. Incident and diffracted X-Rays by the layer of atoms in a crystalline structure | 31 |
| Figure 4.5. Basic concept of X-Ray Diffractometer | 32 |
| Figure 4.6. Basic concept of AFM | 33 |
| Figure 4.7. Allowed Metal Contact Pads on Sample Surface | 34 |
| Figure 4.8. Schematic illustrations of absorption measurements | 36 |
| Figure 4.9. Typical J-V curve of a solar cell | 37 |

| | |
|-------------------------------------------------------------------------------------------------------------------------------------------------------------------------|----|
| Figure 5.1. Cross section of InGaN structure showing layers and their thicknesses..... | 42 |
| Figure 5.2. (a) Band diagram of solar cell structures with fixed In composition (b) and graded In composition | 43 |
| Figure 5.3. Cross section of ud-GaN structure showing layers and their thicknesses | 44 |
| Figure 5.4. Cross section of n-GaN structure showing layers and their thicknesses | 45 |
| Figure 5.5. Cross section of p-InGaN structure showing layers and their thicknesses | 45 |
| Figure 5.6. Cross sectional of the solar cell structures on sapphire substrate showing layers and their thicknesses | 46 |
| Figure 5.7. Typical device fabrication sequence; (a)cross section of solar cell structure, (b) device isolation (c) mesa etching and (d) metal depositions | 49 |
| Figure 5.8. Top views of the fabricated solar cell devices | 49 |
| Figure 6.1. LayTec Reflectance of growing (a) InN , (b) In _{0,93} GaN and (c) In _{0,06} GaN | 51 |
| Figure 6.2. X-ray spectra of In _x Ga _{1-x} N layers (x=0.2:1.0) | 53 |
| Figure 6.3. FWHM values of In _x Ga _{1-x} N layers (x=0.2:1.0) | 54 |

| | |
|-----------------------------------------------------------------------------------------------------------------------------------------------|----|
| Figure 6.4. AFM images of the $\text{In}_x\text{Ga}_{1-x}\text{N}$ layers; (a) $x=0.20$, (b) $x=0.53$, (c) $x=1.00$ | 55 |
| Figure 6.5. Background electron concentration (N_b) and mobility (μ) of InGaN epitaxial layers | 57 |
| Figure 6.6. (a) Reflection + Transmission and (b) Absorption spectra of the InGaN layers with various In content | 58 |
| Figure 6.7. Absorption coefficient of InGaN epitaxial structures with various In composition | 60 |
| Figure 6.8. X-Ray spectra of p- $\text{In}_{0.07}\text{GaN}$ | 62 |
| Figure 6.9. X-Ray spectra of the fabricated solar cell structures | 64 |
| Figure 6.10. (a) Reflection + Transmission and (b) Absorption spectra of the InGaN solar cell structures with various In content | 65 |
| Figure 6.11. Current-voltage characteristics of the fabricated solar cells with different In composition | 66 |

CHAPTER 1

INTRODUCTION

Increasing demand in energy over the past fifty years resulted in a drive for research in clean and commercially viable energy resources. Projection shows that worldwide energy consumption will increase from 13TW (2011) to approximately 30TW by 2050^[1].

Burning non-renewable energy sources such as oil, coal and natural gas releases greenhouse gasses into the atmosphere as by-products. Thus as shown in Figure 1.1, carbon dioxide emission is increasing at a much faster pace than before, particularly due to mankind activities in both industrial and developing countries



World carbon dioxide emissions from fossil fuels 1900–1999 and forecast to 2020 (billion tonnes)

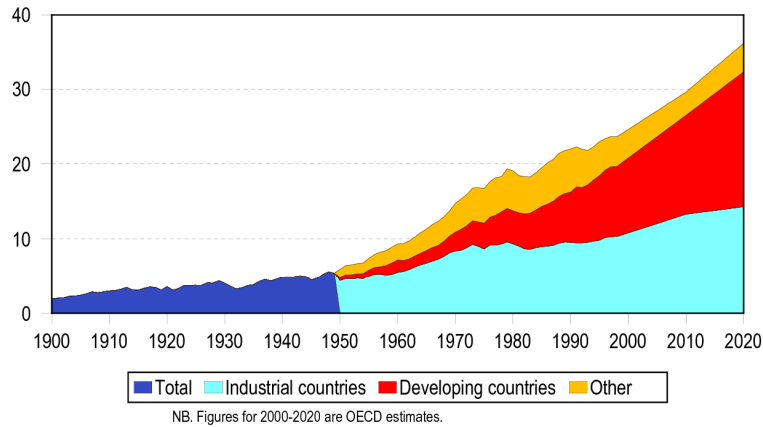


Figure 1.1. Global carbon dioxide emissions from fossil fuels ^[1].

Figure 1.2 shows the consumption of various resources and corresponding oil consumption per year. There is a clear increase in the use of renewable energy sources as shown in the yellow region which belongs to renewable sources such as solar, wind and geothermal.

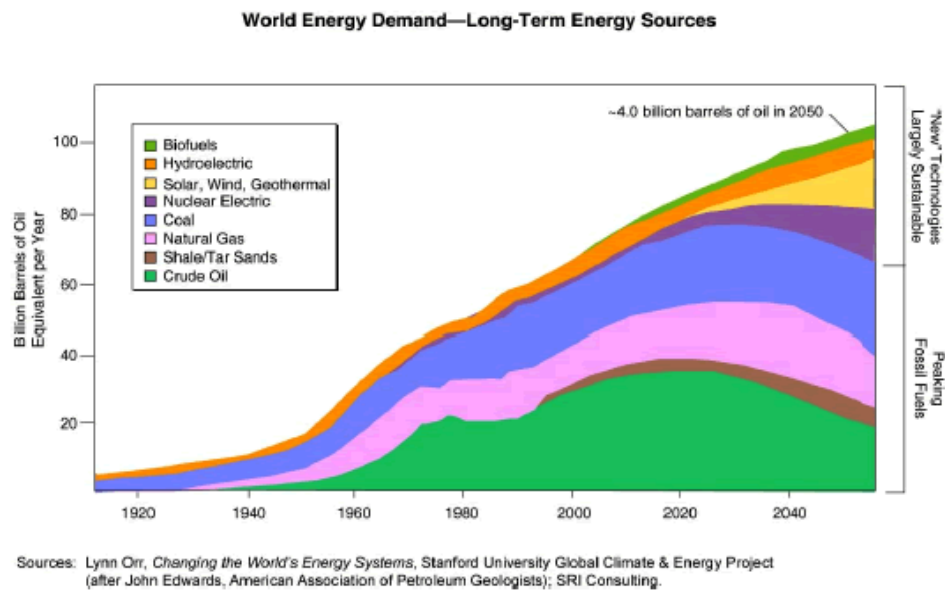


Figure 1.2. Consumption of various resources and corresponding oil consumption [66]

Solar energy was only contributed about $1/10^6$ of total world energy demand in 2006^[3]. But the market is growing rapidly and solar capacity increased more than twice from 2009 to 2010. In 2010, 17GW energy was produced by more than 100 countries with solar capacity, which was only 7.3GW in 2009^[4]. Renewable sources could produce 7% of the total energy consumed worldwide^[5]. Solar energy makes up 2.8%, biomass makes up 10% and hydropower makes up 3.4% of this, meaning that solar technology is the fastest growing power-generation technology.^[5] Harvesting sunlight and converting it into electricity is very desirable due to its abundance and cleanliness. Carbon-free solar energy, which is around 105 TW, could be harvested by photovoltaic devices^[2]. The amount of energy that is provided by sun in one hour is more than the total energy consumption of the world for 1 year^[6, 7].

Solar cells or photovoltaic devices (PV) are designed to absorb sunlight and convert it into usable electrical energy. The PV effect first discovered by A.E.

Becquerel^[8] and then Charles Fritts produced first PV cell with only 1% efficiency in 1883^[9]. Bell Laboratories developed the first modern PV cell using silicon p-n junction in 1954^[10]. Nowadays, the efficiency of crystalline single junction silicon solar cells reaches up to 25%^[11] approaching to their theoretical limit of 33.7% (Shockley Queisser limit)^[12]. These efficiencies belong to sophisticated small scale laboratory production. Mass produced and less expensive market modules produce lower efficiencies in between 15-20 %^[13].

In 2010, large commercial arrays cost down to \$3.40/watt, which was from \$8.00/watt back in 2004^[14]. First generation silicon solar cells are dominating the market; however, they still cost more than desired. Other alternatives that are shown in the Figure 1.3 below may have the potential of yielding higher efficiencies at lower cost.

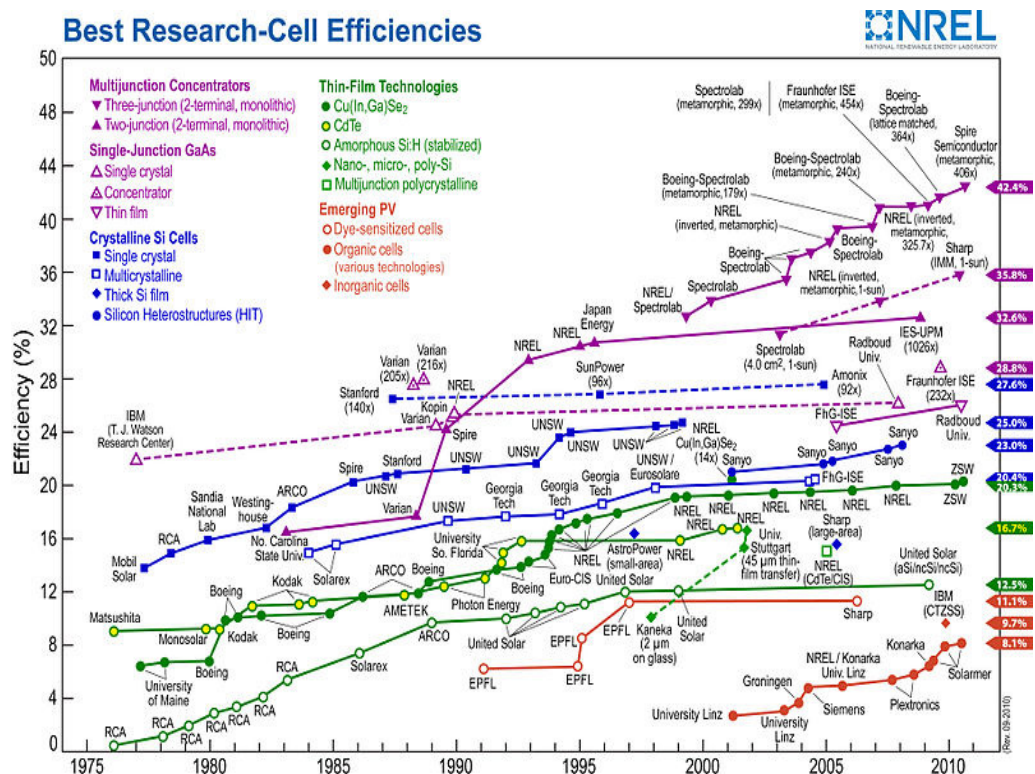


Figure 1.3. Best research cell efficiencies^[15].

The highest solar cell conversion efficiency was obtained by Junqiao Wu using a triple junction of gallium indium phosphide (GaInP), gallium arsenide (GaAs) and germanium (Ge)^[16], which is about 43%. The structure had band gaps of 1.9 eV, 1.4 eV and 0.7 eV, respectively ^[17]. Further increase in efficiency, would need additional junctions. Theoretically, a four junction solar cell can reach an efficiency of around 62% with band gaps of 0.6 eV, 1.11 eV, 1.69 eV and 2.48 eV^[18]. However, increasing the number of junctions introduce difficulties in finding a suitable material with proper bandgaps. Fortunately, III-Nitride alloys offer a great potential to overcome this problem.

1.1. Properties of III-Nitrides

The bandgaps of the III–nitrides are large and direct. The band gap values are ~ 0.7 eV for indium nitride (InN), 3.4 eV for gallium nitride (GaN), and 6.2 eV for aluminum nitride (AlN). Because of their wide bandgaps and high bond strength, they can be used for a variety of devices such as light emitting diodes (LED), high electron mobility transistors that are capable of operating at high temperatures, detectors and solar cells.

Structural, electrical and thermal properties of III-Nitrides obtained from literature are tabulated and provide in Table 1.1. ^{[16], [19], [22], [23], [24]}.

Table 1.1. Properties of group III-nitrides

| Properties | GaN | InN | AlN |
|-------------------------------------------------------------|----------------------------------------------------------------|----------------------------------------------------------------|----------------------------------------------------------------|
| Crystal Structure | Wurtzide | Wurtzide | Wurtzide |
| Melting Point ($^{\circ}\text{C}$) ^[16] | 2791 | 2146 | 3481 |
| Thermal Conductivity(W/cm/C) _[28] | 1.3 | 0.8 | 2 |
| Band Gap (eV @ 300K) ^[16] | 3.43 | ~0.7 | 6.14 |
| Electron Mobility (cm ² /V.s) ^[28] | 900 | 4400 | 300 |
| Hole Mobility (cm ² /V.s) ^[28] | 30 | 39 | 14 |
| Specific Gravity (g/cc) ^[28] | 6.1 | - | 1.95 |
| Specific Heat (J/gmC) ^[28] | 0.49 | 0.32 | 0.6 |
| Thermal Diffusivity (cm ² /s) ^[28] | 0.43 | 0.2 | 0.47 |
| Thermal Expansion Coefficient ^[16] | $\alpha_c=3.2 \text{ E}^{-6}$ $\alpha_a=5.6 \text{ E}^{-6}$ | $\alpha_c=3.8 \text{ E}^{-6}$ $\alpha_a=2.9 \text{ E}^{-6}$ | $\alpha_c=5.3 \text{ E}^{-6}$ $\alpha_a=4.2 \text{ E}^{-6}$ |
| Lattice Constant 'a' (300K) ^[16] | 0.3189 | 0.3533 | 0.3112 |
| Lattice Constant 'c' (300K) ^[16] | 0.5186 | 0.5760 | 0.4982 |
| Dielectric Constant ' ϵ_0 ' ^[28] | 9.5 | 8.4 | 8.5 |

1.2. Application of III-nitrides

Nitride based semiconductors have been used for a wide range of applications such as ^[20, 21].

- Light Emitting Diodes (LEDs),
- Laser Diodes (LDs),
- Transistors for High Temperature/High Power,
- Photodetectors for Solar-Blind UV Detection,
- Solar Cells.

1.3. Substrates

Since there is a lack of commercially available native substrates, there have been various efforts to develop substrates for III-nitride deposition systems. GaN is the most studied member of the nitride family and most of the problems arise from lattice and thermal mismatch to GaN. Dislocations and stacking faults do arise from lattice mismatch and thermal mismatch causes epilayer cracks that occur during cooling process. III-Nitrides mainly grown on sapphire, Si, silicon carbide (SiC) and rarely on GaN. Additionally zinc oxide (ZnO), magnesium aluminate (MgAl₂O₄), gallium arsenide (GaAs), magnesium oxide (MgO), sodium chloride (NaCl) and titanium dioxide (TiO₂) have also been investigated ^[24]. Semiconductor materials with various bandgaps and crystal constants are shown in the Figure 1.4. These values It should be taken into account when considering material growth on different epitaxial structures and substrates.

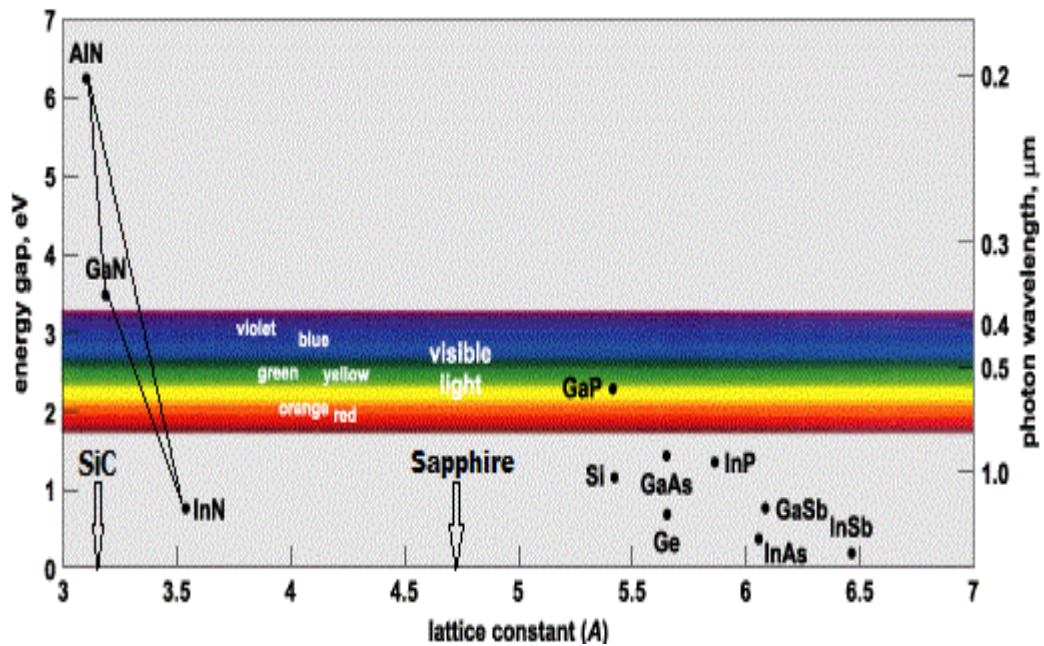


Figure 1.4. Crystal constants and bandgaps for various semiconducting materials

[26].

1.4. Growth Techniques

The biggest problem is to find a suitable substrate for the epitaxial growth of III-nitrides, since the bulk growth of III-nitrides has not been developed yet to produce substrates for homoepitaxy. Thus, III-nitride epitaxial growth still needs to be performed on foreign substrates (heteroepitaxy) that have lattice and thermal mismatch between substrate and growing epitaxial layers. Most common substrates for epitaxial growth of III-Nitrides are sapphire and SiC. Although SiC is a better match to III-nitride films it is not widely available, due to its high cost compared to that of sapphire.

Since foreign substrates have large mismatch with the growing III-Nitride films, one should find unique solutions for high quality III-Nitride materials for device applications. Liquid Phase Epitaxy (LPE), Molecular Beam Epitaxy (MBE) and MOCVD are some of the epitaxial methods for the deposition of III-Nitrides. [24].

- **Liquid Phase Epitaxy (LPE)**

In LPE growth, thin film layers are grown on a seed crystal or solid substrates from their molten material. Growth rate depends on the cooling process. LPE process has fast growth rate and low production cost. On the other hand, growth of complex material systems is difficult since different molten sources are needed within the same deposition system and substrate has to be transferred between those molten sources. This growth technique is not suitable for film thicknesses lower than 1 mm^[25].

- **Molecular Beam Epitaxy (MBE)**

In MBE growth, epitaxy takes place in ultra high vacuum (10^{-8} Pa) and the sources are heated separately. It is possible to precisely control the temperature of the individual sources. With the help of a MBE system, ultra pure materials can be grown. Ultra high vacuum levels required for the deposition increases the cost of fabrication. Due to the low deposition rate and high operation cost of the MBE systems is not suitable for mass production.

- **Metal Organic Chemical Vapor Deposition (MOCVD)**

There are several different MOCVD systems (Nitride-based, As-based, P-based and etc.) for the deposition of materials. The material system that is desired to be deposited determines the system configuration, primarily including sources and reactor design. There are metal-organic sources such as trimethylgallium (TMGa), triethylgallium (TEGa), trimethylaluminium (TMAI), trimethylindium (TMIIn), silane (SiH_4), that are carried by carrier gasses like hydrogen or nitrogen through a well organized piping system to a reactor and sent through the substrate, following proper mixing and heating. MOCVD growth method is suitable for mass production since it grows high purity materials and allows the use of multiple substrates at a time. Batch production decreases the running costs of the system.

CHAPTER 2

METAL ORGANIC CHEMICAL VAPOR DEPOSITION (MOCVD) METHOD

2.1. Epitaxy

Epitaxy has Greek roots that consist of ‘epi’ which means upon and ‘taxis’ which means ‘arranged’. The term ‘epitaxial growth’ covers the film growth on a crystalline substrate in an ordered manner where the atomic arrangement of the grown film accepts crystallographic structure of the substrate. In other words, it could simply be the deposition of a monocrystalline film on a monocrystalline substrate. Epitaxial growth is one of the most important techniques that allows the production of various kinds of optoelectronic devices. These sophisticated devices require a number of thin film structures with various contents, stoichiometries and thicknesses.

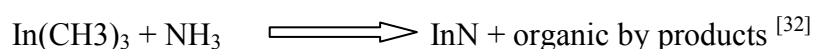
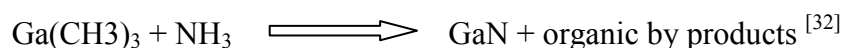
- Homoepitaxy; crystalline film is grown on a substrate of the same material (i.e. Si thin film on Si substrate)
- Heteroepitaxy; crystalline film and substrate are different from each other (i.e. GaN thin film on sapphire substrate)

2.2. MOCVD Growth Technique

MOCVD growth technique have been in use for the deposition of epitaxial thin films for more than thirty years. As/P based, SiC based and GaN based materials can be deposited with MOCVD method. Growth temperature for As/P based materials system is around 850 °C [26], where GaN based material systems need higher growth temperatures around 1100 °C [27]. Typically, nitrogen or hydrogen gas is used as a carrier gas. MOCVD technique is the best method for the deposition of multilayer structures of III-nitrides and widely used for mass production. Depositions of AlGaIn/GaN and InGaIn/GaN structures for various device applications have been widely investigated using MOCVD method [28].

This growth technique utilizes gas mixtures that contain the molecules to be deposited called ‘precursors’, to grow epitaxial thin films. The carrier gas, high purity hydrogen or nitrogen, has to be chosen according to the growing material [29].

Figure 2.1 shows the sequence of steps during a typical MOCVD growth. There are four regions as seen in the figure. The gas mixture, containing all the necessary molecules for the material growth, is coming from the left side to the heated substrate. Sources that are in the gas mixture diffuse down to the substrate. Diffused precursors react with each other and following necessary chemical interactions, desired materials are grown on the substrate that is indicated in the figure [29]. Chemical reactions between precursors are [32]:



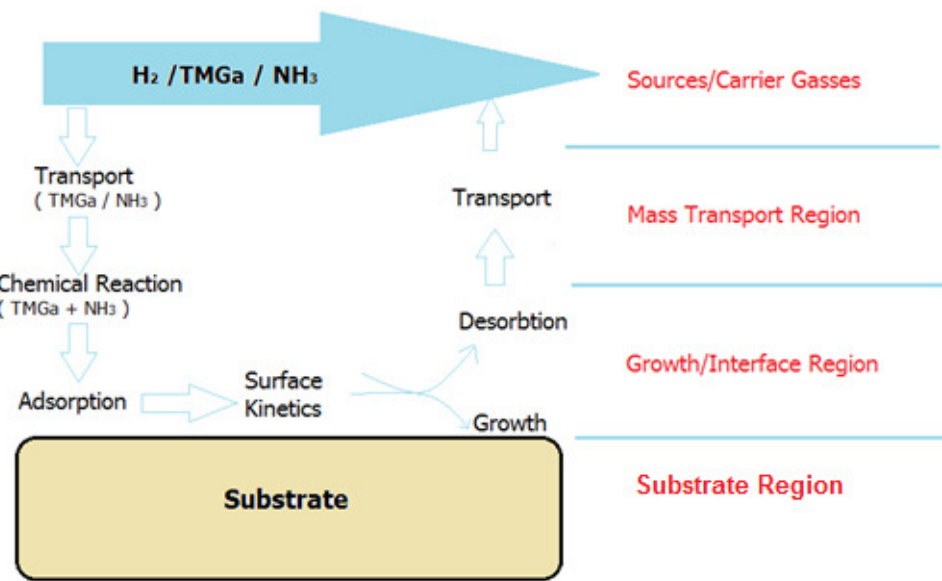


Figure 2.1. Schematic steps for MOCVD growth.

Molecules that are adsorbed by the surface of the substrate are not fixed on the surface; instead they are mobile. Surface kinetics is not fully understood yet due to the lack of in-situ measurement tools.

2.2.1. Configuration

Figure 2.2 shows a simple schematic diagram of a MOCVD system where only sources and related pipelines are shown. The sources that are used during growth follows the necessary lines to reach up to the reactor and others that are not used during growth falls into the ‘Vent Line’. MOCVD system also uses various kinds of electronic and pneumatic valves, mass flow controllers, pressure controllers and switching systems for the atomic scale control of the growing materials simply by precisely adjusting the amount of sources flowing towards the reactor^[29].

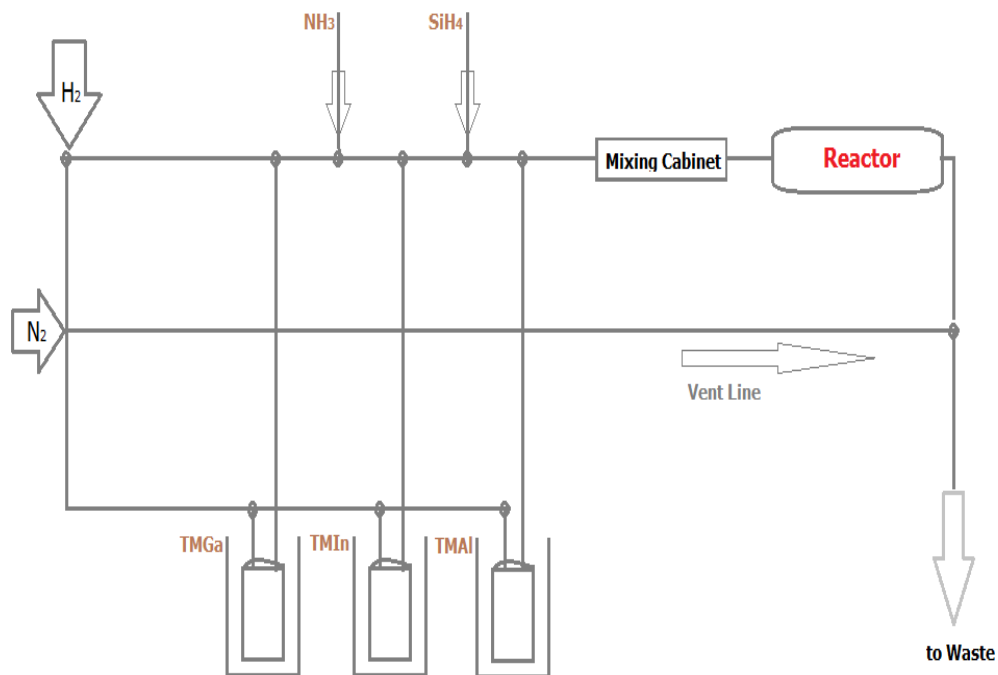


Figure 2.2. Schematics diagram of a MOCVD system.

Figure 2.3 shows a simple schematic diagram of a horizontal MOCVD reactor. The sources and carrier gasses (H_2 or N_2) pass through the 'Gas Inlet' and reach the reactor. There is a 'Rotating Susceptor' that carries the wafer holder. Rotation helps to improve the uniformity of growing epitaxial layers. Heating of the reactor can be done by several methods. RF coil around the reactor, as shown in the schematic, provides a uniform temperature gradient across the wafer. This has prime importance for epi-growth.

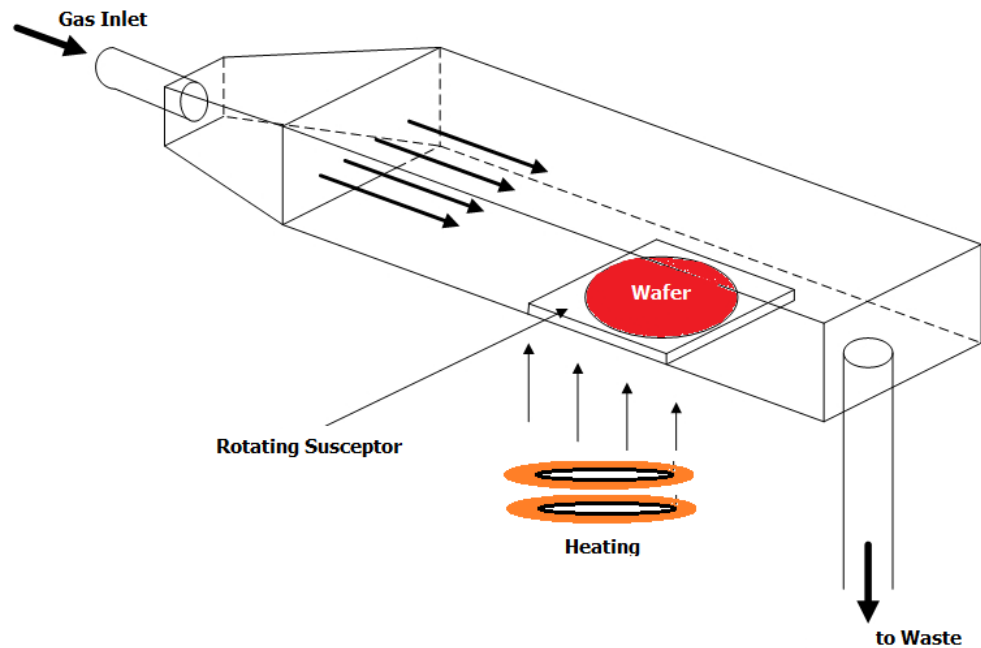
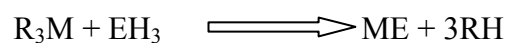


Figure 2.3. Schematic diagram of MOCVD reactor ^[29].

2.2.2. Sources

Wide range of available source materials is one of the biggest advantages of MOCVD system over those other thin film deposition methods. In MOCVD growth, generally alkyls of the group II and III metals and hydrides of group V and VI elements are used. Diluted vapors of these sources are transported to a reactor at high temperatures, where the pyrolysis reaction takes place for epitaxial thin film growth.

In general, pyrolysis reaction can be generalized for III-V materials as follows ^[8]:



, where R, M and E are the alkyl radicals (C₂H₅ or CH₃), the group III metals (Ga, In, Al) and the group V element (N, P, As, Sb), respectively.

Table 2.1. Sources of MOCVD system ^[30].

| Name of Compound | Acronymy | Purpose |
|--------------------------------|--------------------------------|----------------|
| Trimethylgallium | TMGa | III element |
| Triethylgallium | TEGa | III element |
| Trimethylaluminium | TMAI | III element |
| Triethylaluminium | TEAI | III element |
| Trimethylindium | TMIIn | III element |
| Triethylindium | TEIn | III element |
| Ethyl-dimethylindium | EDMIIn | III element |
| Trimethylantimony | TMSb | V element |
| Triethylantimony | TESb | V element |
| Trimethylarsine | TMAAs | V element |
| Dimethylarsinehydride | DEAs | V element |
| tert-Butylarsine | TBAAs | V element |
| tert-Butylphosphine | TBP | V element |
| Arshine | AsH ₃ | V element |
| Phosphine | PH ₃ | V element |
| Hydrogen Selenide | H ₂ Se | n-dopant |
| Hydrogen Sulfide | H ₂ S | n-dopant |
| Silane | SiH ₄ | n-dopant |
| Disilane | Si ₂ H ₆ | n-dopant |
| Tetramethylin | TMSn | n-dopant |
| Tetraethylin | TESn | n-dopant |
| Dimethylzinc | DMZn | p-dopant |
| Diethylzinc | DEZn | p-dopant |
| Diethylberyllium | DEBe | p-dopant |
| Dimethylcadmium | DMCd | p-dopant |
| Bis-cyclopentadienyl magnesium | BCp ₂ Mg | p-dopant |

Criteria for those source materials listed in Table 2.1 are ^[30]:

- stability at room temperature,
- vaporization in N₂, H₂ or He without decomposing,
- lowest possible toxicity,
- purification possibility for impurity removal,
- resistance to spontaneous decomposition or polymerization.

Since a number of the sources are available for MOCVD system, this technique is more flexible than other epitaxial growth techniques.

In MOCVD system, trimethyl sources are most often used due to their higher vapor pressure and stability compared to others. It is also important to choose metal organic and hydride sources that could easily decompose at the growth temperature of the desired material systems.

CHAPTER 3

SOLAR CELL DESIGN

3.1. Conversion of Solar Energy

The energy for a solar cell is coming from the sun. This energy input depends on several variables like wavelength of the incident light, atmospheric conditions, latitude and time of the day. This energy input is converted into current and voltage by a solar cell. Passing through the atmosphere, solar radiation is absorbed by the gases those are constituents of the atmosphere. The radiation spectra in Figure 3.1 show the impinging power per area (m^2) with respect to wavelength (nm). The solar spectrum outside the atmosphere is shown by AM0, and AM1.5 is used for solar radiation that is tilted 48° with respect to the surface normal on the earth. Both AM1.5G and AM1.5D is for terrestrial applications; but, AM1.5D includes only direct light, where AM1.5G includes both direct and diffuse light ^[31].

The amount of incident light to be converted into electrical energy by a solar cell mostly depends on the solar cell materials and microfabrication processes that were used for the fabrication of solar cells. To increase the number of the incident photons trapped within the material, bandgap of the material should be chosen properly corresponding to a portion of the solar spectrum.

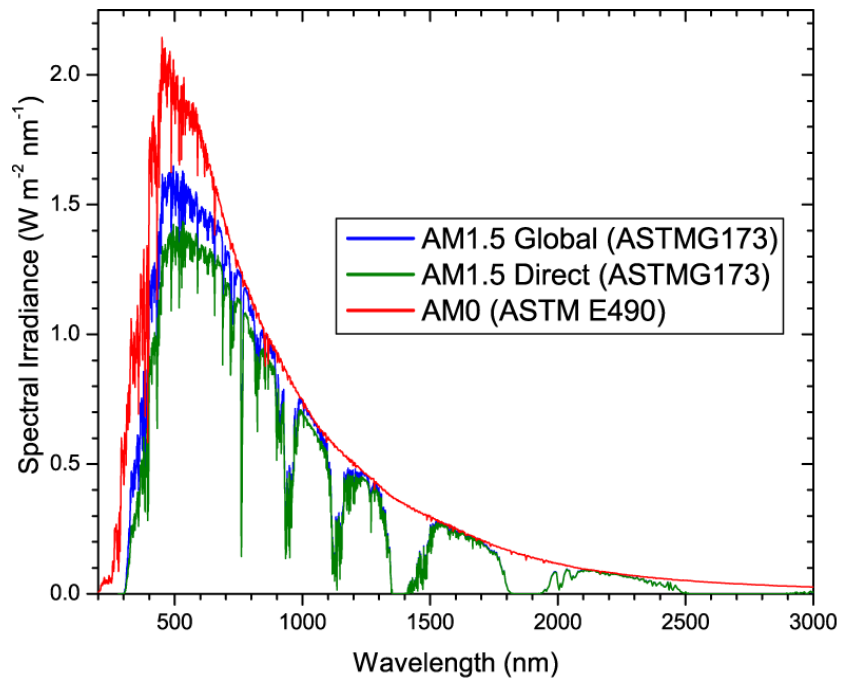


Figure 3.1. Solar spectrum ^[31].

3.2. Band Diagram of a Solar Cell

Solar cells consist of a junction that is formed between p and n-type semiconductors. These semiconductors could either be the same material (homojunction) or different materials (heterojunction). Band structures of the individual doped materials are shown in Figure 3.2 ^[32].

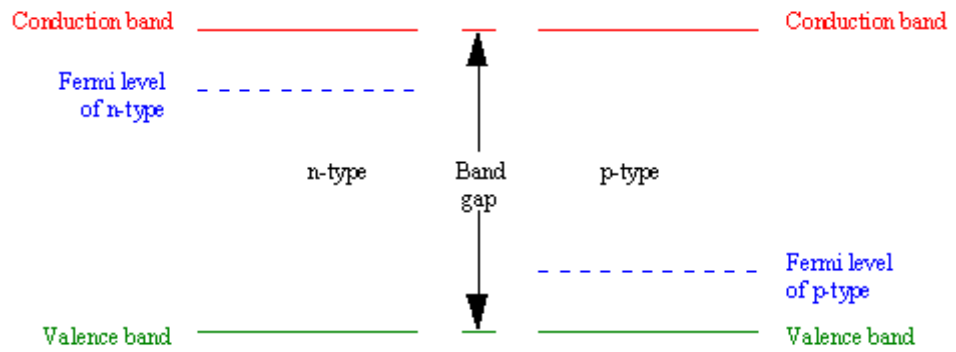


Figure 3.2. Energy band structure of a n and p-type doped semiconductor.

When two differently doped semiconductors are brought together, Fermi levels of the semiconductors are forced to equilibrate, which causes band bending and formation of a ‘depletion region’ as shown in Figure 3.3 ^[32].

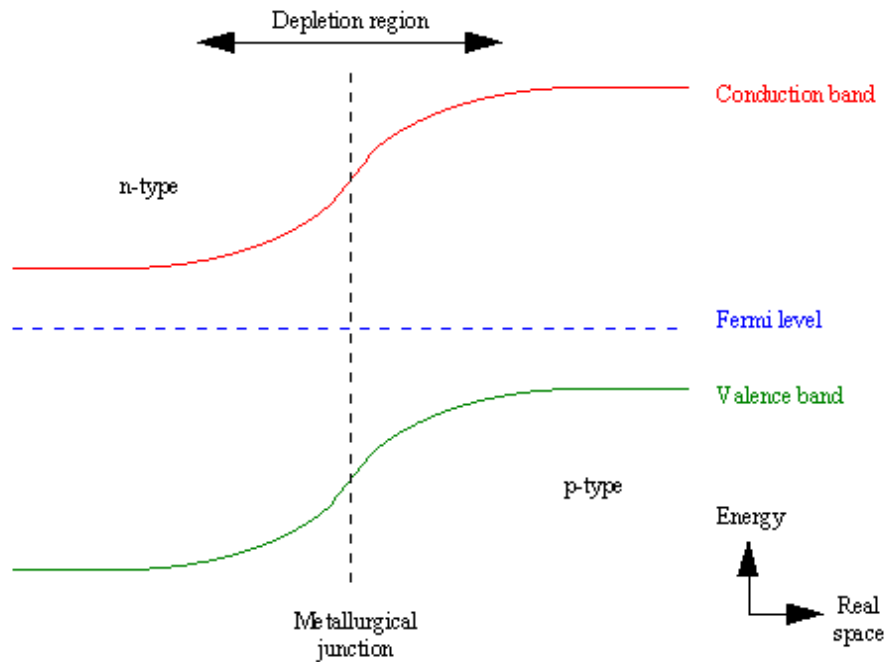


Figure 3.3. Energy band structure of a p-n heterojunction.

A photon with energy higher than the bandgap of the semiconductor could generate an electron/hole pair. This kind of absorption is known as ‘band to band’ electronic transition. If produced electron/hole pairs could travel to the depletion region before they recombine, they are separated by the ‘built in electric field’, which helps carriers to get collected by contacts and flow through external loads. This process, shown in Figure 3.4, is the origin of the solar cell’s photocurrent^[32].

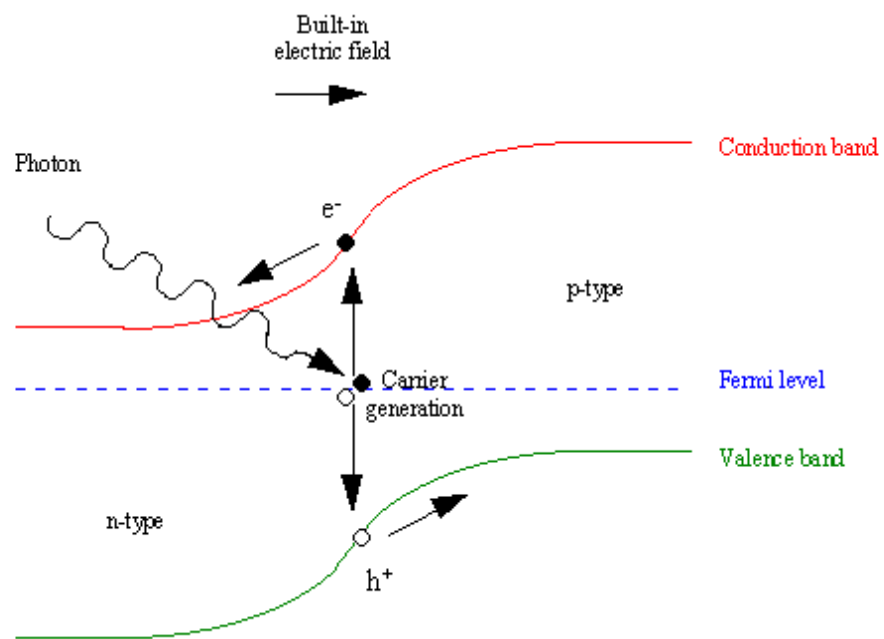


Figure 3.4. Basic operation principle of a solar cell^[32].

3.3. Solar Cell Structure

In general, inorganic semiconductors are used to form suitable junctions for solar cells that show a PV effect upon illumination. Large number of inorganic semiconductors exhibit PV effect; but, only few of those materials have commercial interest. The ideal solar cell material should have a direct bandgap of magnitude 1.5 eV, and high optical absorption coefficient ($\sim 10^5 \text{ cm}^{-1}$), high

quantum efficiency of excited carriers and long diffusion length. The optimum thickness of an absorption layer in a solar cell depends on the order of the inverse of the optical absorption coefficient of the material. A material with high optical absorption coefficient must be a thin film ^[33].

A solar cell is made up of a p-n junction. A typical p-n junction solar cell structure consists of a top layer or emitter (n-type semiconductor), a base layer (p-type semiconductor), electrodes and anti-reflection coating (ARC). ARC is used to reduce reflection losses. The top electrode within the structure should be transparent or in grid structure to allow the incoming photons to penetrate into the active layer for charge carrier generation ^[31]; but, thick enough at the same time to minimize series resistance. Schematic illustration of a single junction solar cell is given in Figure 3.5.

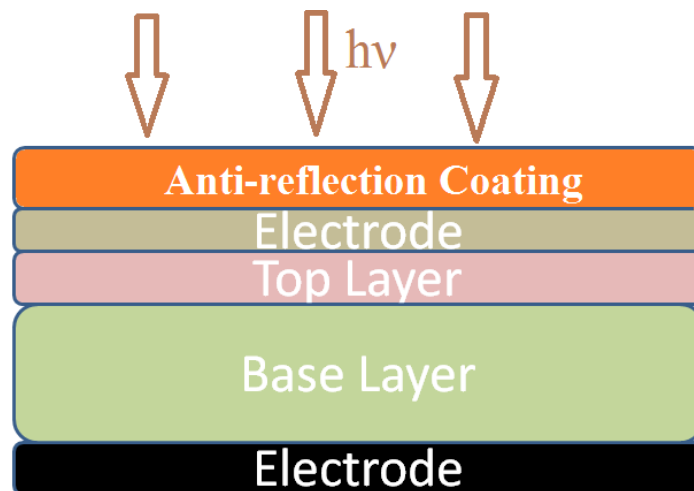


Figure 3.5. Cross section of a solar cell.

3.3.1. Single Junction Solar Cells

Solar cell structure that includes only one junction is called ‘single junction’ solar cell.

The highest efficiency for a single junction solar cell is about 28% (obtained for GaAs thin film solar cell) demonstrated by National Renewable Energy Laboratory (NREL) ^[34].

3.3.2. Tandem Solar Cells for High Efficiency

Major losses of solar cells are due to thermalization and below bandgap photons of the solar spectrum. These losses could be largely eliminated if the incoming photons have energies slightly higher than the bandgap of the cell material. This idea results in the concept of a tandem cell, where several cells are used in series with different bandgaps. In this case, each individual cell is responsible for the conversion of a portion of the solar spectrum that is close to its bandgap ^[35]. Simple schematic of a tandem solar cell design is shown in Figure 3.6.

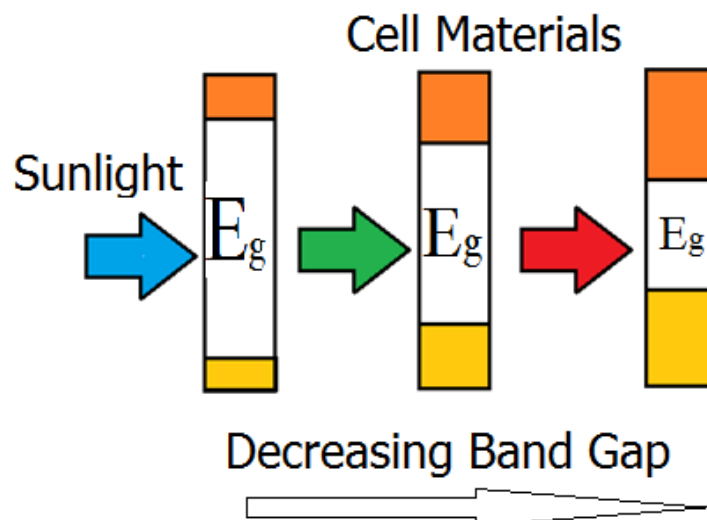


Figure 3.6. Tandem solar cell concepts ^[35].

High bandgap materials stacked on very top of the structure absorbs the energetic photons and transmits photons that are absorbed by lower bandgap materials located below. With the help of the tandem cell concept, greater portion of the spectrum could be covered by the solar cell leading to an increase in conversion efficiency.

The resulting efficiency of a solar cell could be increased by stacking several solar cells with different bandgap energies, so that the maximum theoretical efficiency could reach up to 86.8% [36].

Figure 3.7 (a) and (b) shows the solar spectrum (AM1.5) and the portion of the solar spectrum covered by a single junction Si solar cell and triple-junction solar cell, respectively.

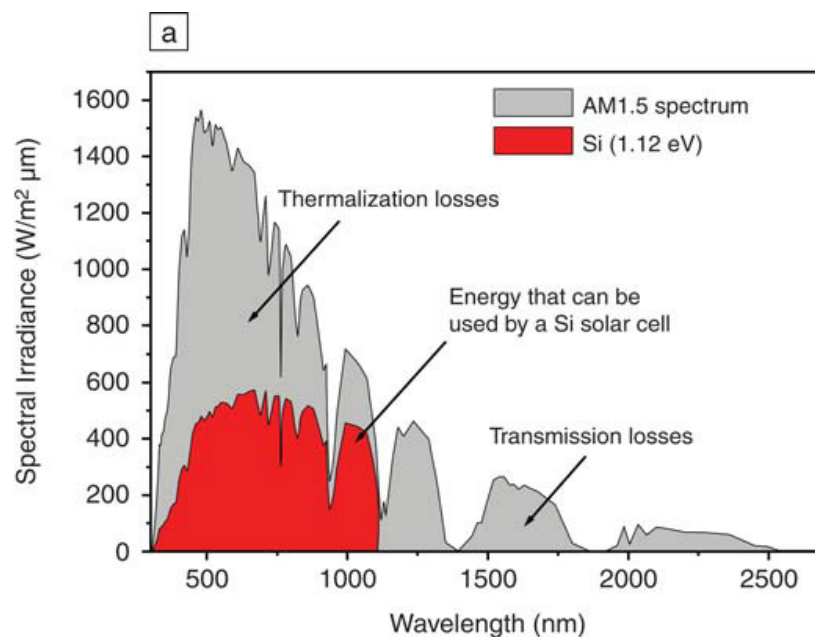


Figure 3.7. AM1.5 spectrum and parts of the spectrum that can be used by (a) Si solar cell and (b) triple-junction solar cell [36].

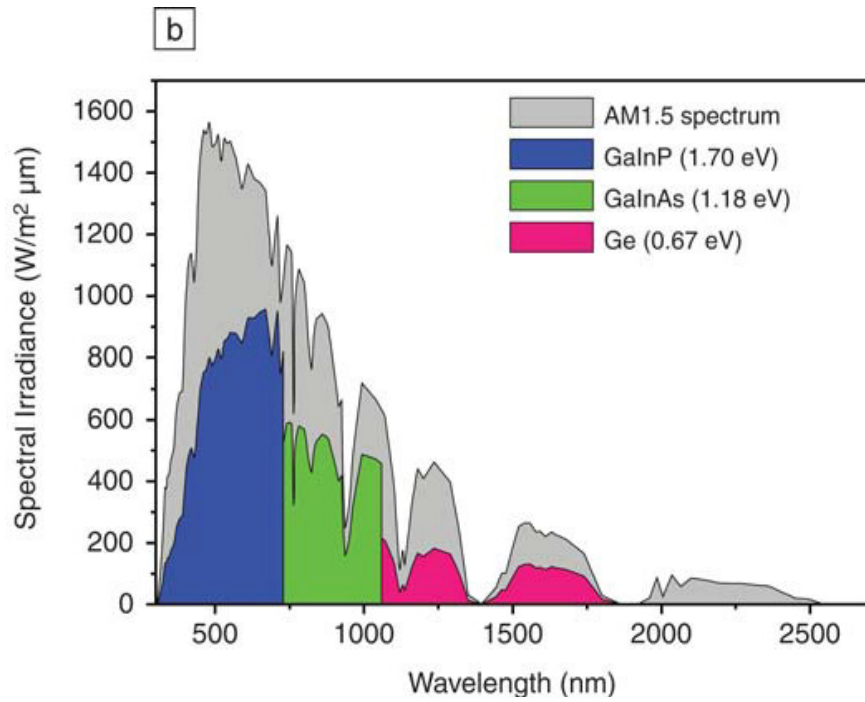


Figure 3.7. AM1.5 spectrum and parts of the spectrum that can be used by (a) Si solar cell and (b) triple-junction solar cell ^[36] (continued).

Figure 3.8 shows the portion of the covered solar spectrum by individual solar cells within the tandem structure. It is seen that the number of the epitaxial layers in a tandem solar cell is greater than twenty.

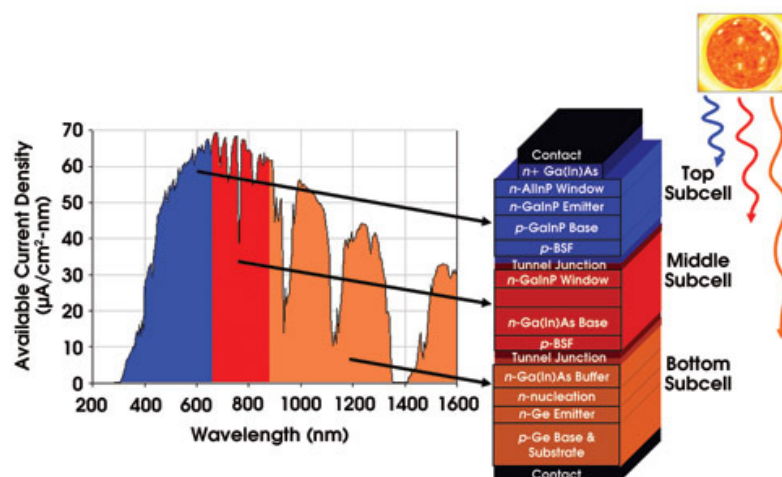


Figure 3.8. Multi junction solar cell structure and covered solar spectrum ^[37].

Figure 3.9 show the bandgap of the materials along with their lattice constants. There is a big difference in lattice constants between nitride material systems and other system as shown in Figure 3.9.

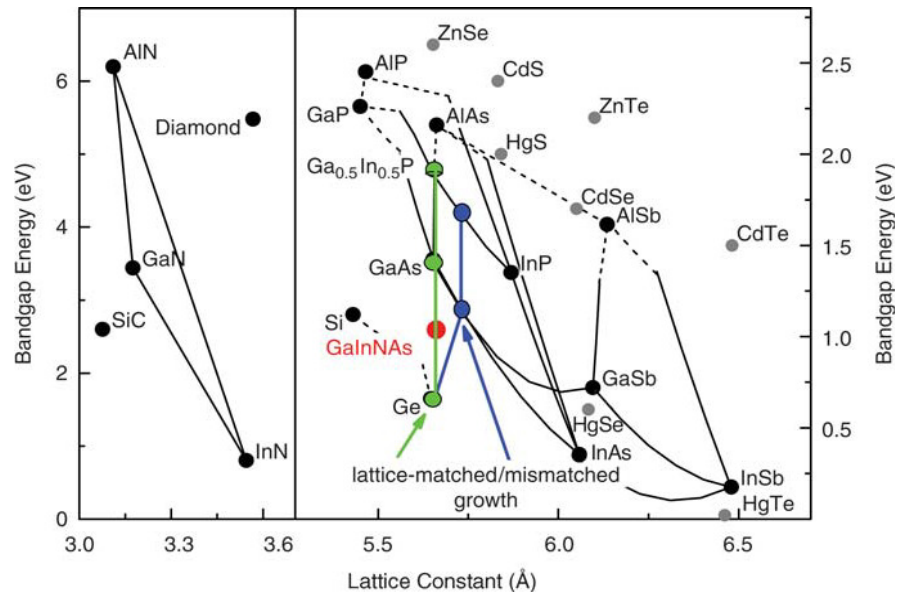


Figure 3.9. Bandgaps of the materials as a function of their lattice constant [36]

It is not that easy to grow these epitaxial structures especially when the differences in lattice and thermal constants have been taken into account. These are the main drawbacks for the growth of tandem solar cells.

3.3.3. InGaN Material System

Theoretical calculations [38], as in Table 3.1, have already been carried out using ‘Rapid Flux Calculation Method’. Results revealed that several materials with different bandgaps are required to build a multi junction solar cell to increase the efficiency. Hence, it can be seen that such solar cells require bandgaps larger than 2.00 eV to reach 50% or excess in efficiency.

Table 3.1. Theoretical efficiency calculation for a tandem solar cell that have materials with different bandgaps^[38].

| n | E ₁ | E ₂ | E ₃ | E ₄ | E ₅ | E ₆ | E ₇ | E ₈ | n (%) |
|---|--------------------------|----------------|----------------|----------------|----------------|----------------|----------------|----------------|-------|
| | AM1.5 G spectrum (1sun) | | | | | | | | |
| 1 | 1.34 | | | | | | | | 33.68 |
| 2 | 0.94 | 1.60 | | | | | | | 45.71 |
| 3 | 0.94 | 1.37 | 1.90 | | | | | | 51.58 |
| 4 | 0.71 | 1.11 | 1.49 | 2.00 | | | | | 55.31 |
| 5 | 0.70 | 1.01 | 1.33 | 1.67 | 2.14 | | | | 57.61 |
| 6 | 0.69 | 0.96 | 1.20 | 1.47 | 1.79 | 2.24 | | | 59.41 |
| 7 | 0.69 | 0.93 | 1.14 | 1.37 | 1.60 | 1.90 | 2.33 | | 60.78 |
| 8 | 0.51 | 0.75 | 0.98 | 1.18 | 1.40 | 1.63 | 1.92 | 2.35 | 61.42 |

InGaN, a III-Nitride material system, has several unique properties that would allow the fabrication of high performance solar cells with low cost. Since, wide bandgap materials are needed in multijunction solar cell structures to achieve ultrahigh efficiencies (> 50%), InGaN could be one of those. InGaN alloy is one of the few materials that have a bandgap greater than 2.4 eV, and it can be tuned between 0.7 eV (InN)^[39] and 3.4 eV (GaN). In addition to the wide bandgap, InGaN alloy has a direct bandgap and strong absorption coefficient that makes it an ideal candidate for multijunction solar cells^[39].

As seen from the Figure 3.10, InGaN material system covers much of the solar spectrum opposed to InGaP and AlGaAs systems.

THE SOLAR SPECTRUM

Indium gallium nitride absorbs more of the Sun's energy than today's best alternatives

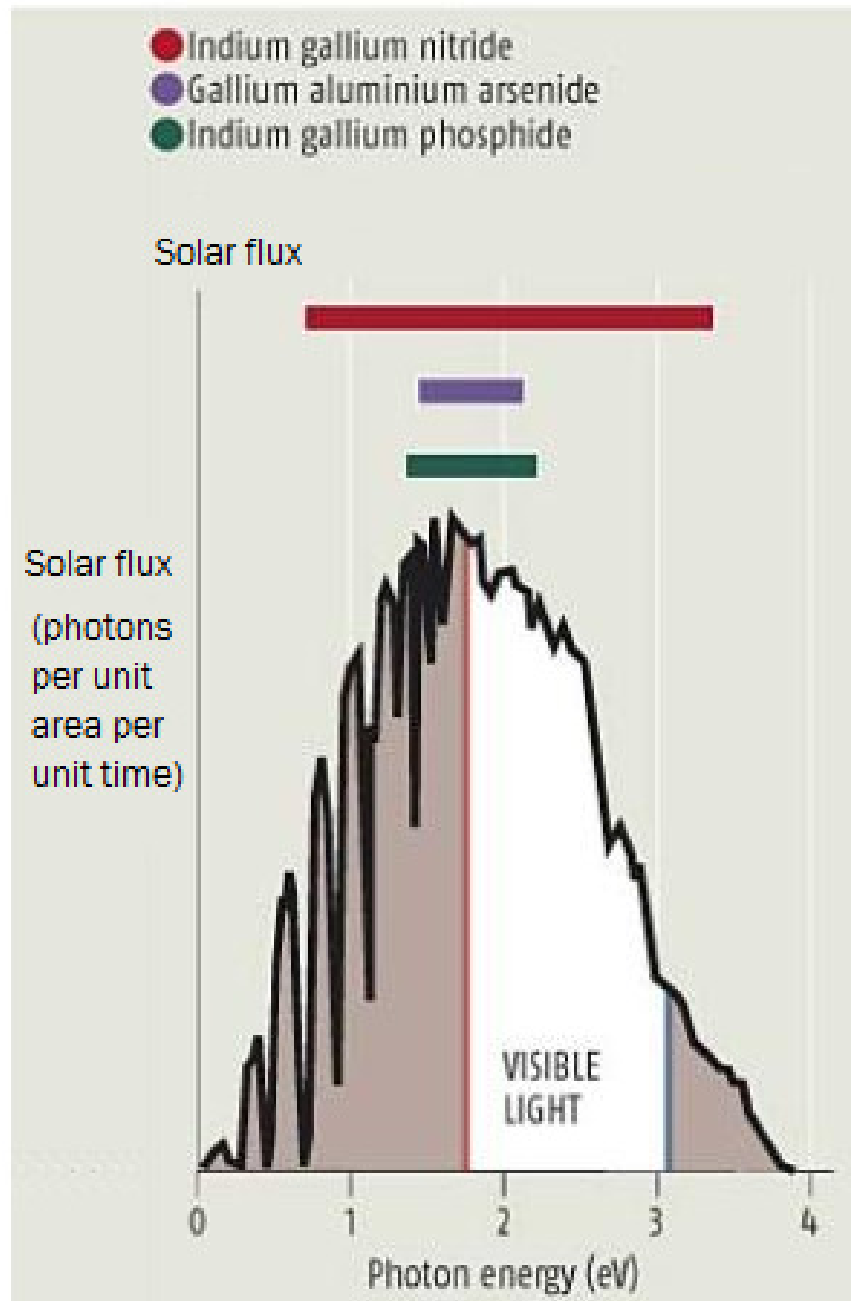


Figure 3.10. Solar spectrum for III-V solar cells ^[41].

CHAPTER 4

CHARACTERIZATION TECHNIQUES

4.1. In-situ Characterization

Epitaxial growth is not only the first step for manufacturing optoelectronic devices but also a determining factor for device performance. Therefore, precise control of the growth parameters is crucial.

Optical reflectance measurements could be used to investigate material properties like growth rate, layer thickness, composition of ternary alloys and surface roughness^[41].

Schematic of the in-situ optical reflectance setup is shown in the Figure 4.1;

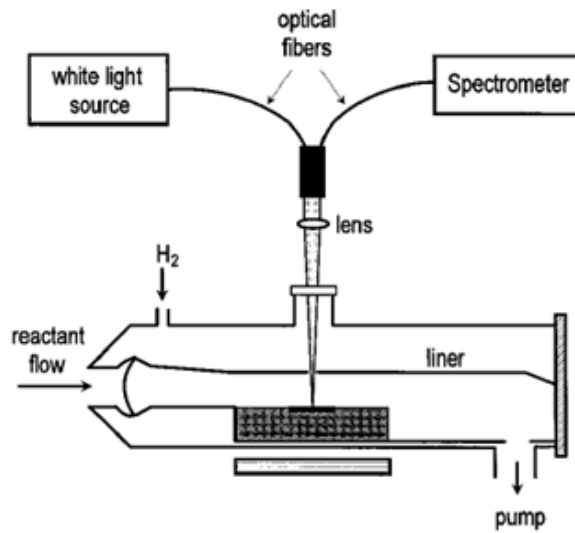


Figure 4.1. Schematic for in-situ reflectance measurement setup ^[45].

In this system, light of a certain wavelength impinges on the layer that is growing and partly reflected back to the spectrometer.

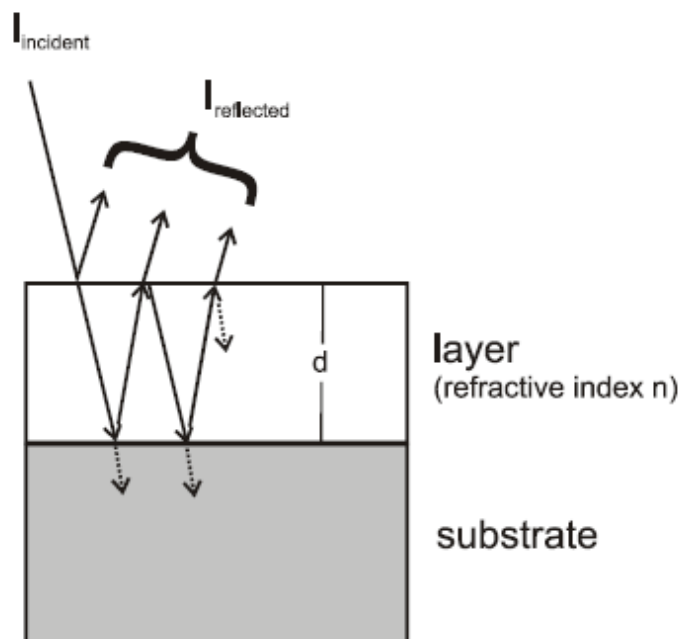


Figure 4.2. Reflection of light from surfaces ^[45].

The phase difference of the reflected light depends on the wavelength of the incident light, optical constant and layer thickness of the deposited material. For normal incidence, constructive and maximum reflectance occur if the path difference between two beams equal to an even number of half wavelength. Destructive interference and minimum reflectance occur when the path difference between two beams equal to an odd number of half wavelength

$$2nd = m\lambda \rightarrow \text{constructive interference and maximum reflectance}^{[45]}$$

$$2nd = (m+1/2)\lambda \rightarrow \text{destructive interference and minimum reflectance}^{[45]}$$

, where n is the refractive index, d is the thickness of the layer, λ is the wavelength of the incident light and m is an even number.

The influence of the surface quality on the intensity of the reflected light for growing materials is shown in Figure 4.3. Reflectance of ideal growth, material with increasing thickness and material with increasing surface roughness are shown in Figure 4.3 (a), (b) and (c), respectively. The tendency of the reflectance oscillation not only depends on the surface roughness but also depends on the growing film thicknesses.

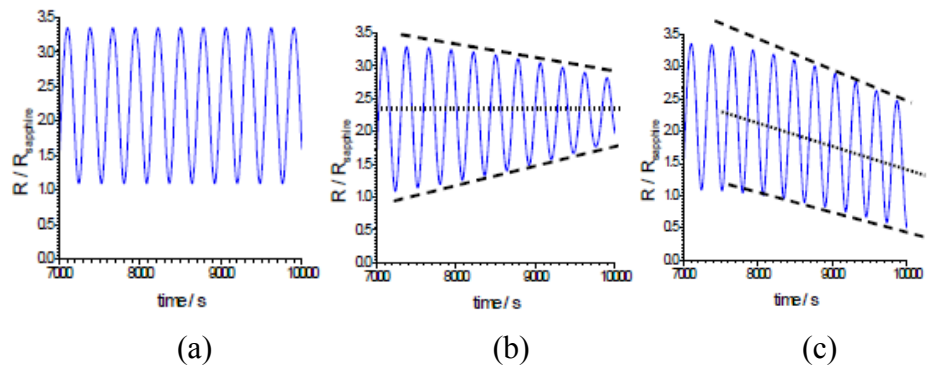


Figure 4.3. Reflectance of a) ideal growth, b) increasing material thickness and c) increasing surface roughness^[41].

4.2. X-Ray Diffraction

One of the nondestructive ex-situ measurement methods used to investigate the epitaxial thin film quality is X-Ray Diffraction (XRD) analysis. Information that is gathered from diffraction pattern is used to identify the layer composition, uniformity, thickness, strain states and crystal imperfections related to their dislocation density.

XRD is based on constructive interference of monochromatic X-Rays scattered by a crystalline sample. These X-Rays are generated by a cathode ray tube, filtered for monochromatic radiation, collimated to a concentrated beam and finally directed towards the sample. A Typical ray diagram of incident and scattered beams are shown in Figure 4.4.

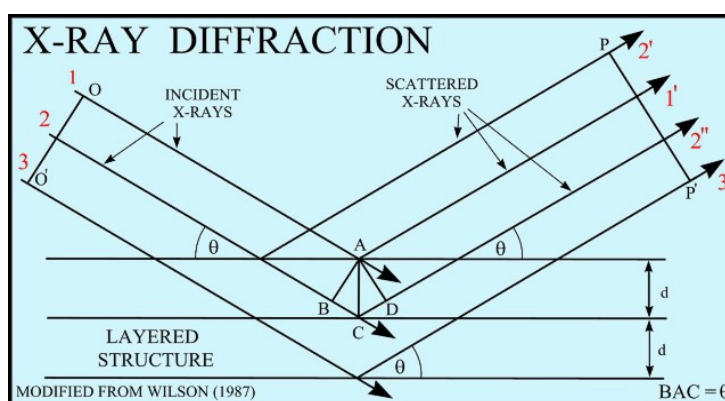


Figure 4.4. Incident and scattered X-Rays by the layer of atoms in a crystalline structure ^[67].

X-Rays have wavelengths on the order of a few angstroms ($1\text{\AA} = 0.1\text{ nm}$). That is similar to the inter-atomic distance (d) in crystalline solids, which allows scattering of X-Rays from the amount of crystalline materials. Schematics of XRD diffractometer and layout of components are shown in Figure 4.5.

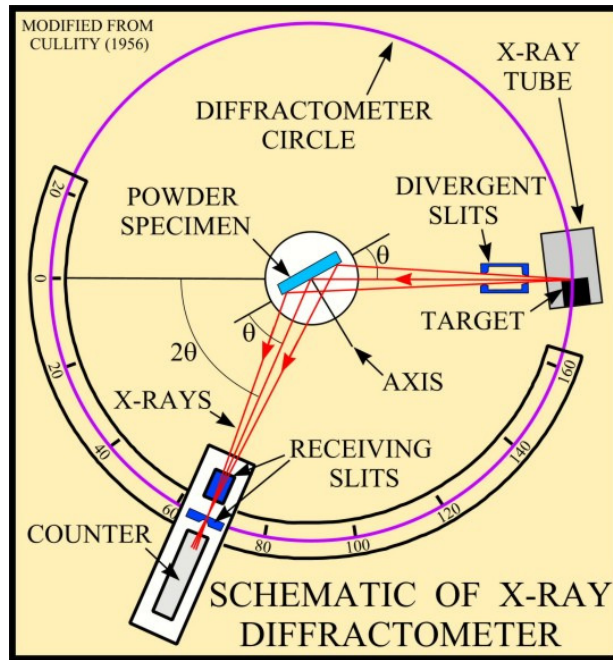


Figure 4.5. Basic concept of X-Ray Diffractometer ^[67].

Interaction of the incident X-Rays with the sample produces constructive interference of the diffracted X-Rays only at certain angles that satisfies Bragg's Law: :

$$2d \sin(\theta_B) = n\lambda \quad (4.1.)$$

, where d is the interplanar spacing, λ is the wavelength of the X-Rays, n is the order of reflection and θ_B is the Bragg's angle. Determination of θ_B reveals the d of the crystal phase, and in turn the lattice parameter.

4.3. Atomic Force Microscopy (AFM)

Atomic force microscopy (AFM) is used to investigate the surface profile of thin films at nanoscale. A cantilever with a fine tip is rastered over the thin film of interest. Upon an obstacle encounter (i.e. surface features) it deflects. The deflection of the cantilever is tracked by a laser. This deflection gives information about thin film surface. Schematics of an AFM is shown in Figure 4.6.

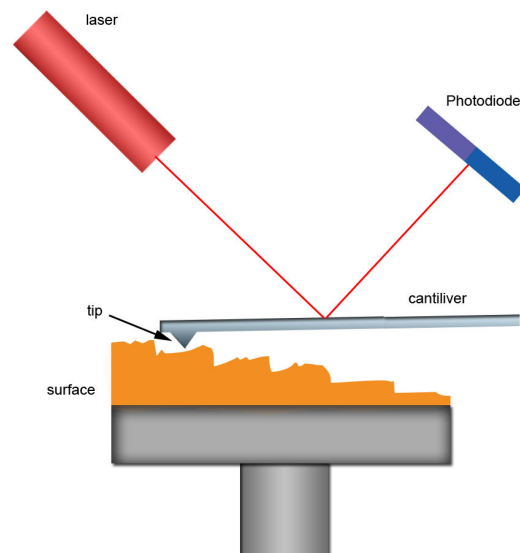


Figure 4.6. Basic schematics of AFM setup

4.4. Hall-Effect Measurements

Hall-effect is a simple analysis method to determine the electrical properties of semiconductors. Hall-effect measurement gives the resistivity, mobility and the carrier concentration type of the semiconductor. Using four ohmic contacts in Van Der Pauw geometry as shown Figure 4.7, the sheet resistance (R_s) of the

semiconductor could be calculated by measuring the resistance across the horizontal and vertical sides using eq.4.2. Options for preparing proper contact pads are shown in Figure 4.7.

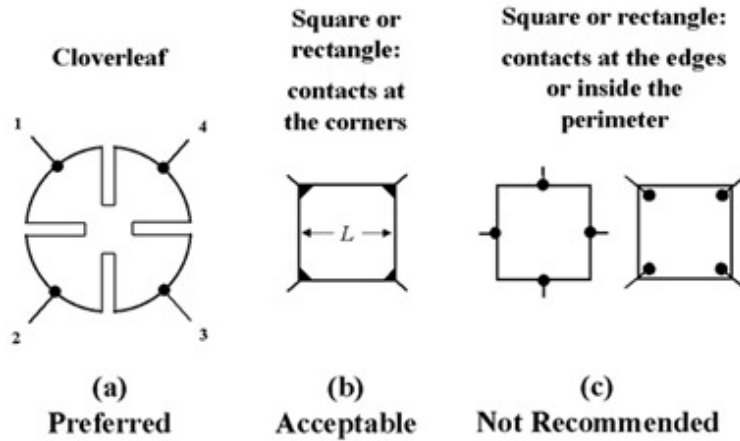


Figure 4.7. Allowed metal contact pads on sample surface

$$e^{-\pi R_{\text{vertical}}/R_s} + e^{-\pi R_{\text{horizontal}}/R_s} = 1 \quad (4.2.)$$

, where R_s is the sheet resistance, R_{vertical} is the resistance across the vertical sides and $R_{\text{horizontal}}$ is the resistance across the horizontal sides of the sample.

Assuming an n-type material, such that $\mu_n n \gg \mu_p p$, the relationship between sheet resistance and electron mobility can be written as ; ^[25].

$$R_s = \frac{1}{qn_s \mu_n} \quad (4.3.)$$

$$\mu = \frac{1}{qn_s R_s} \quad (4.4.)$$

To determine the mobility and carrier concentration, Van der Pauw method is used, which is divided into two parts; resistivity and Hall measurements. Resistivity measurements are done by applying a voltage across one edge of the sample and measuring the current flowing along the opposing edge.

For Hall Measurements a known magnetic field is applied perpendicular to the current flowing in the sample. This results in a voltage orthogonal to both the current and magnetic field, called Hall Voltage. From Hall voltage, carrier concentration and mobility could be calculated^[25].

$$V = \frac{IB}{qn_s} \quad (4.5.)$$

, where I is current, B is the strength of magnetic field, q is the elementary charge and n_s is the sheet density of the majority carriers.

4.5. Absorption Measurements

Light absorption occurs when atoms or molecules take up the energy of an incoming photon. Thus, electromagnetic energy is transformed to other forms of energy. Absorbance (A) is defined as the negative logarithm of transmittance (T), where I_0 and I_1 are the intensity of incident light and transmitted light, respectively.

$$T = \frac{I_1}{I_0} \quad (4.6.)$$

$$A = -\log T \quad (4.7.)$$

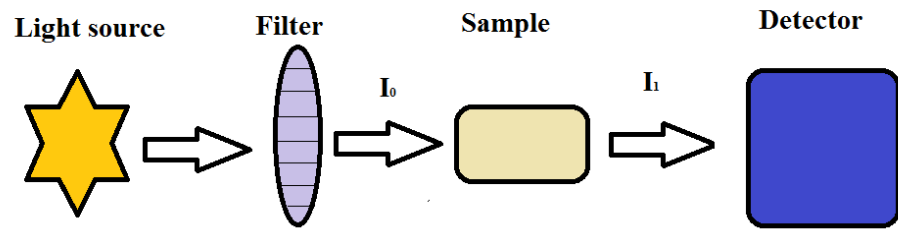


Figure 4.8. Schematic illustration of absorption measurement.

It is also possible to derive the absorption coefficient ‘ α ’ of the epitaxial layer through Beer-Lambert law;:

$$T = \frac{I_1}{I_0} = 10^{-\alpha l} \quad (4.8.)$$

, where l is the thickness of the material.

4.6. Solar Cell Characterization

Electrical performance of a solar cell could be determined by current density versus voltage (J-V) measurements, which is the most common technique in photovoltaics. In general, measurement is carried out upon illumination with AM1.5G spectrum (see Figure 3.1). Figure 4.9 shows a typical J-V characteristic of a solar cell under illumination, where important points like open circuit voltage (V_{oc}), short circuit current density (J_{sc}), voltage at the maximum power point (V_{mmp}) and the current density at the maximum power point (J_{mmp}) are marked on the figure.

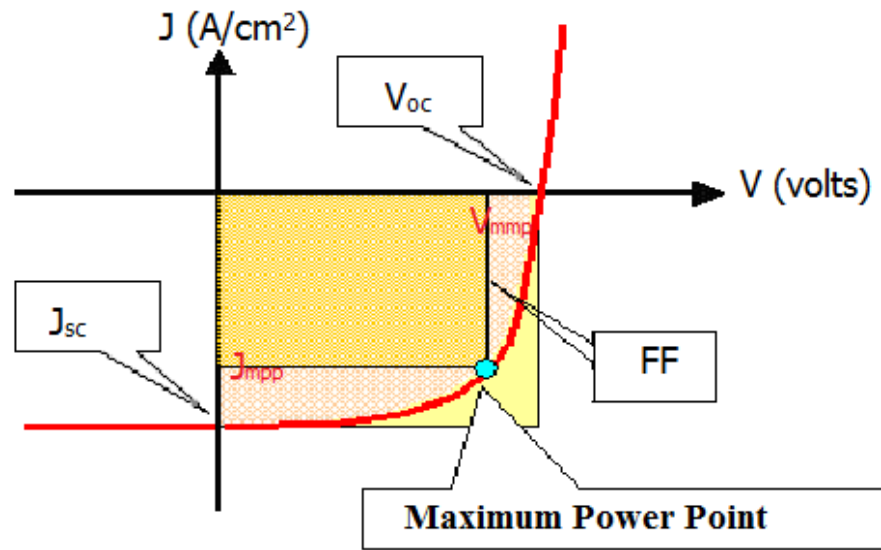


Figure 4.9. Typical J-V curve of a solar cell.

The J_{sc} is current density at $V=0$ and V_{oc} is the voltage at $J=0$. When a solar cell is illuminated, it produces power in the enclosed area at the fourth quadrant as seen from Figure 4.9. The maximum power that is produced by the solar cell at the maximum power point (mmp);

$$P_{mmp} = J_{mmp} V_{mmp} \quad (4.9.)$$

The fill factor (FF) is defined by the ratio of power produced at the maximum power point divided by the product of V_{oc} and J_{sc} :

$$FF = \frac{J_{mmp} V_{mmp}}{J_{sc} V_{oc}} \quad (4.10.)$$

The efficiency of a solar cell is then calculated by dividing output power at maximum power point (P_{mpp}) to incident power density (P_{in}) where P_{in} is equal to 100 mW/cm^2 for AM1.5G spectrum.

$$\eta = \frac{P_{out}}{P_{in}} = \frac{J_{sc} V_{oc} FF}{P_{in}} \quad (4.11.)$$

Series Resistance

The resistance of the metal contacts, bulk resistance of the semiconductor and the resistance due to metal/semiconductor interfaces all add to a total resistance called series resistance. Solar cell performance decreases with increasing series resistance. Magnitude of the series resistance can simply be calculated from J-V characteristic:

$$R_s = \frac{1}{\frac{dI}{dV}} \quad \text{at } V = V_{oc} \quad (4.12.)$$

Shunt Resistance

The leakage current across the junction is a measure of shunt resistance. This leakage may occur due to the manufacturing defects of the semiconductor. A high shunt resistance is desired to minimize leakage current. Magnitude of the shunt resistance can simply be calculated from J-V characteristic:

$$R_{sh} = \frac{1}{\frac{dI}{dV}} \quad \text{at } V = 0 \quad (4.13.)$$

Ideality Factor (n)

The ideality factor (n) of a diode is a measure of how closely the diode follows the ideal diode equation.

$$I = I_s \left[\exp\left(\frac{qV}{nkT}\right) - 1 \right] \quad (4.14)$$

, where I_s is the saturation current, q is the elementary charge, V is the voltage, k is the Boltzmann factor, T is the absolute temperature and n is the ideality factor.

For an ideal solar cell series resistance (R_s) should be lower as much as possible in the order of ohm/sq in order to collect carriers efficiently. Shunt resistance (R_{sh}) should be highest as much as possible to avoid any leakage through alternative conductive pads. In order to increase R_{sh} devices should be passivated with a proper material. The magnitude of the ideality factor should be around 1 or as close as possible to that value.

CHAPTER 5

EXPERIMENTAL DETAILS

5.1. In rich InGaN Thin Film Growth by MOCVD

High quality InGaN growth suffers from the instability of In atoms, low InN binding energy and large lattice mismatch between InGaN and GaN layers. Segregation is another problem during the growth of high quality InGaN layers^[42]. InGaN alloys can cover the solar spectrum from near UV to infrared region since their bandgaps can be tuned in the range of 0.7 eV (InN) to 3.4 eV (GaN)^[46].

InGaN material is the most mystic one in group III-nitrides, many problems arise due to In, which makes the growth of high quality InGaN notably difficult. Calculated In-N binding energy is 1.98 eV which is lower than that of Ga-N (2.20 eV) and Al-N (2.88 eV). Weak binding energy means lower growth temperature for In incorporation and higher decomposition rates at high growth temperatures. This would decrease the In content in InGaN layers^[43]. In order to increase the In content, growth temperature has to be decreased. On the other hand, quality of InGaN epilayer decreases at low growth temperatures due to insufficient diffusion of metal atoms and lower ammonia decomposition rate^[44].

Lower In incorporation with increasing growth temperatures needs higher In flow for InGaN growth, which complicates stoichiometry control. At higher In flow rates, In segregations increase, which deteriorates the InGaN epilayer quality^[42].

To pressurize In segregations in InGaN layers, In flow needs to be kept as low as possible while increasing V/III ratio ^[45]. On the other hand, low In flow increases surface roughness of the InGaN layer. To have high quality InGaN epilayer, In segregations and rough surfaces should be avoided.

Crystal constants are also problematic considering InGaN growth. Lattice mismatch between InGaN and GaN increase with increasing In content in the InGaN layer. If the thickness of InGaN layer exceeds a critical value then strain in the layer is relieved by means of dislocations and cracks during cooling, degrading the device performance^[42].

In this work, the growth of epitaxial layers were performed using an AIXTRON 200/4 RF-S MOCVD system. TMGa, TMIIn, TEGa and NH₃ were used as a source materials and hydrogen and nitrogen gases were used as carrier gases. InGaN epitaxial growths were initiated with GaN nucleation layer at 575 °C, TMGa flow was set to 10 sccm, NH₃ flow was 1500 sccm and growth pressure was 200 mbar. The layer thickness was around 10 nm. Then, GaN buffer layer was started at 1070 °C, TMGa flow was set at 15 sccm and NH₃ was 1800 sccm under the same growth pressure. A total GaN thin film thickness of 2.6 μm was obtained. Identical GaN buffer layer was used for all InGaN growths. For InGaN layers, temperature was varied between 550-745 °C, while keeping V/III ratio higher than that of GaN. The growth pressure was set to 200 mbar for all the growth experiments. We changed both V/III ratio (mainly In flow) and temperature to have different In content within InGaN layers. For InN growth, TMIIn flow was set at 10 sccm, NH₃ flow was 1000 sccm, where V/III ratio was around 6.6×10^4 . Temperature and pressure were set to 550°C and 200 mbar, respectively. Matsuoka et al. ^[47] reported higher V/III ratio (6.2×10^5) for InN growth since they used lower growth temperatures. For higher In composition (~90 % In in InGaN layer), TEGa flow was set between 5 and 15 sccm, TMIIn flow was set to 100 sccm, where V/III ratio was around 5700. The growth temperature was 550°C and for lower In composition (~6 %In in InGaN layer) TEGa flow was set at 90 sccm, TMIIn flow to 10 sccm. The growth

temperature was increased to 745 °C, where V/III ratio was around 1.1×10^4 . The growth pressure was kept the same (200 mbar) for all growth runs.

Schematic of the deposited layers with respective layer thicknesses are shown in Figure 5.1. The cross-section schematic reveals the InGaN epitaxial layer that is grown on GaN buffer layer, where sapphire wafer was used as the substrate for all growth experiments.

| |
|--------------------------------------------------|
| InGaN Layer $t \sim 100 - 200\text{nm}$ |
| GaN Buffer Layer $t \sim 2.6 \mu\text{m}$ |
| GaN Nucleation Layer (NL) $t \sim 10 \text{ nm}$ |
| Sapphire Substrate (c-plane) |

Figure 5.1. Cross-section of InGaN structure showing layers and their respective thicknesses.

5.2. InGaN Solar Cell Design

5.2.1. Band Simulations for InGaN Solar Cell

Nextnano semiconductor software solution program was used by Dr. Marek WESOTOWSKI from Institute of Electronic Materials Technology Poland for InGaN solar cell design. Simulations showed that to avoid spikes in the band diagram it is better to use graded passing layer between n and p-region. These spikes, which are shown in Figure 5.2, acts as recombination centers, deteriorating the efficiency of the solar cells.

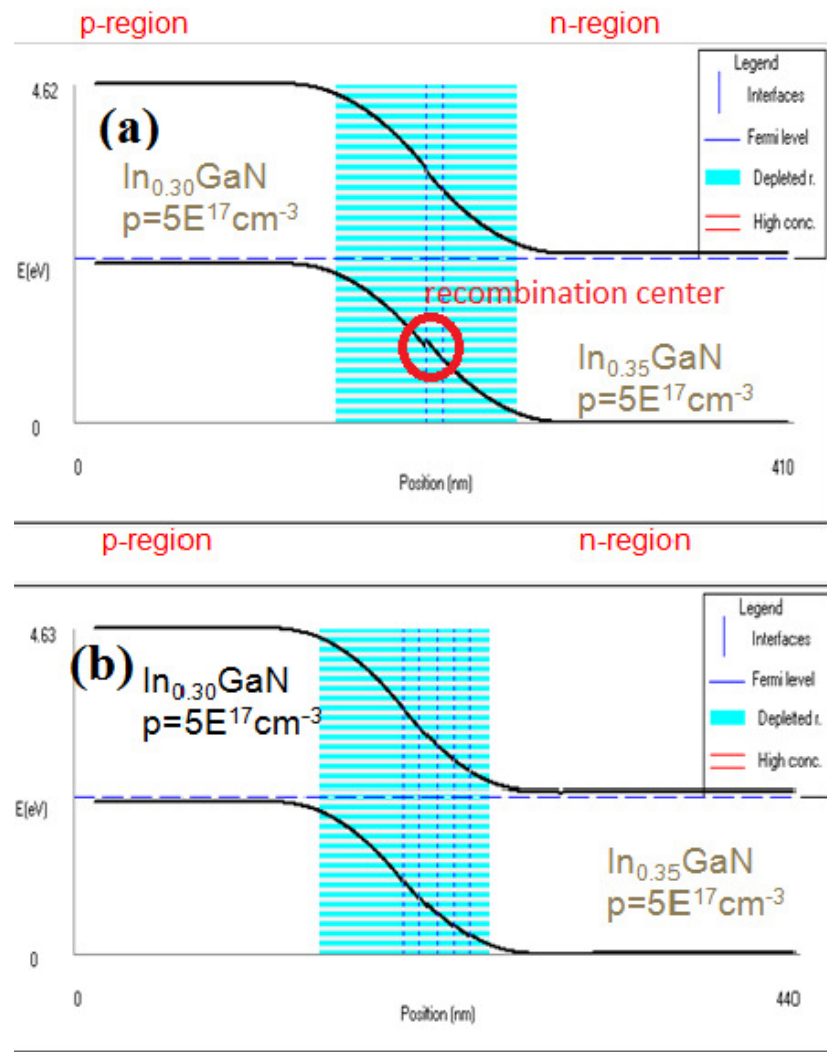


Figure 5.2. (a) Band diagram of solar cell structures with fixed In composition, (b) and graded In composition.

Using graded structure is not only removes recombination center but also to be expected to improve quantum efficiency of solar cell devices. In order to improve the quantum efficiency in CIGS^[74] and silicon-germanium solar cell structures^[75] graded structures were used. Same idea is applied to current study to have graded InGaN active layers in order to increase quantum efficiency of solar cells. Additionally simulations showed that lightly doped graded InGaN layers also increase efficiency of InGaN solar cell^[76].

5.2.2. Preliminary Growth

Basically, the InGaN solar cell structure is comprised of a buffer layer, n-region, i-region (active region) and p-region on the top of the structure. Additional growths were performed for detailed characterization of both n and p-regions.

Buffer layer: ud-GaN layer

All solar cell structures have identical ud-GaN layer, which was grown on a 2'' double side polished (DSP) c-plane sapphire substrate. In order to check the quality of ud-GaN structure, individual growth experiments were performed. Cross-sectional schematics of the buffer structure are shown in Figure 5.3. XRD and Hall measurements were conducted for characterization.

| |
|----------------------------------------------|
| ud-GaN Buffer Layer $t \sim 2.6 \mu\text{m}$ |
| GaN NL $t \sim 10 \text{ nm}$ |
| Sapphire Substrate (c-plane) |

Figure 5.3. Cross-sectional schematic of ud-GaN structure showing layers and respective thicknesses.

n-region: n-GaN Layer

All solar cell structures have identical n-GaN layer, which was grown on ud-GaN layer. In order to check the quality of n-GaN structure, individual growth experiments were performed. Cross-sectional schematic of the structure is shown in Figure 5.4. XRD and Hall measurements were conducted for characterization.

| |
|-------------------------------------------|
| n-GaN Buffer Layer t ~ 1.4 μm |
| ud-GaN Buffer Layer t ~ 1.7 μm |
| GaN NL t ~ 10 nm |
| Sapphire (c-plane) |

Figure 5.4. Cross-sectional schematic of n-GaN structure showing layers and respective thicknesses.

p-region: p-InGaN Layers

The solar cell structures include identical p-InGaN layers. In order to check the quality of p-InGaN structures, individual p-InGaN layers were grown on highly Resistive (HR) GaN templates. Cross-sectional schematic of the structure is shown in Figure 5.5. XRD and Hall measurements of p-InGaN layer were conducted for characterization.

| |
|------------------------------------------|
| p-InGaN t ~150 nm |
| ud-GaN Buffer Layer t ~1.5 μm |
| AlN Buffer Layer t ~ 300 nm |
| AlN NL t ~ 10 nm |
| Substrate Sapphire (c-plane) |

Figure 5.5. Cross-sectional schematic of p-InGaN structure showing layers and respective thicknesses.

5.2.3. InGaN Solar Cell Growth

InGaN solar cell structures were grown on sapphire substrates. Before each growth run, substrates were heated to 1100°C for 10 min under H₂ flow for cleaning.

Following cleaning process, epitaxial growth was started with GaN NL at 575°C, TMGa flow was 10 sccm, NH₃ flow was 1500 sccm and growth pressure was 200 mbar where the layer thickness was around 10 nm. Then GaN buffer layer was started at 1070°C, TMGa flow was 15 sccm and NH₃ was 1800 sccm at the same growth pressure where layer thickness about 1.6 μm. Growth continued with turning on the SiH₄ source, one of the n-type dopant source materials, to have a n-GaN layer. In our MOCVD system we have a dilute line for SiH₄ source and flows for *Source Material*:10 sccm, *Dilute Line*: 1000 sccm and *Inject*: 20 sccm were used. For InGaN layers flow parameters were varied in between 550-745°C, TEGa: 10-100 sccm, TMIn: 10-50 sccm, NH₃: 1000-5000 sccm. p⁺-InGaN layer was grown by just turning on Mg source, which was set at 35 sccm, while keeping all other sources for InGaN layer open. Mg flow was then increased up to 40 sccm to get the final layer p⁺⁺-InGaN layer. The InGaN layers that were used for the active layer had a graded profile to avoid any bandgap discontinuities. Cross-sectional schematic of the solar cell structure grown on c-plane sapphire substrate is shown in Figure 5.6.

| |
|---------------------------------------------------------------------------------------|
| p ⁺⁺ - GaN Layer t~20 nm |
| p ⁺ - In _{x2} GaN Layer t~50 nm |
| In _{x2} GaN Layer t~20 nm |
| graded In _{x1→x2} GaN Layer t~160 nm where x ₁ >x ₂ |
| In _{x1} GaN Layer t~20 nm |
| n-GaN Layer t~1.2 μm |
| ud-GaN Buffer t~1.6 μm |
| GaN NL t~10 nm |
| Sapphire substrate (c-plane) |

Figure 5.6. Cross-sectional schematic of the solar cell structures on sapphire substrate showing layers and respective thicknesses.

5.3. Fabrication of Solar Cell

Before device fabrication, solar cell structures were annealed at 550°C for 15 min under N₂ ambient for Mg activation. Mg activation temperature for p-InGaN layers was typically low to avoid any lattice rearrangement in InGaN layers.

A typical device fabrication sequence is shown Figure 5.7. Standard acetone-isopropanol cleaning was used to clean the wafer before fabrication and in between each fabrication step.

Photolithography: Most important part of the microfabrication on photolithography, in which the desired patterns are defined on the wafers. Therefore, it is required in each step of microfabrication.

Photolithography processes typically include the following steps. First a photoresist (MicroChemicals GMBH: AZ@5214 E), which is sensitive to UV light is coated to the wafer surface. Through UV illumination over a photomask, desired patterns were transferred to the photoresist. Afterwards, a developer (MicroChemicals GMBH: AZ 400K Developer) is used to remove the part of the photoresist that was exposed to UV radiation. Typically, developer solution is used in a 1:4 dilution with deionized water (DI). Then etching or metal deposition could be performed on the patterned photoresist.

A Karl Suss MA6 photolithography equipment was utilized in the microfabrication processes.

Etching: It is one of the basic steps of microfabrication. Many of the device structures consist of thin film layers that are stacked on top of each other. In order to make a contact to deeper layers, etching is necessary.

Inductively coupled plasma reactive ion etches (ICP RIE, Sentech SI 500) instrument and BCl₃, Cl₂ and Ar gasses were used as etching gasses.

Deposition: Deposition processes were performed under vacuum in order to avoid any contamination, which would affect the quality of deposited materials. Metal deposition for the fabrication of electrical contacts and dielectric coatings for electrical isolation are typically used in microfabrication.

A Leybold Univex Electron Beam Evaporation system was used for metallization. Ti (10 nm)/Al (20 nm)/Au (20 nm) alloys were used for the n-side and Ni (40 nm)/Au (150 nm) alloys were used for the p-side contacts. Following metal depositions, n-side contacts were annealed at 550°C for 1 min and p-side contacts were annealed at 530°C for 1.5 min. Typical device fabrication sequence, cross-sectional and top-view images of the fabricated devices are shown in Figure 5.7 and 5.8, respectively.

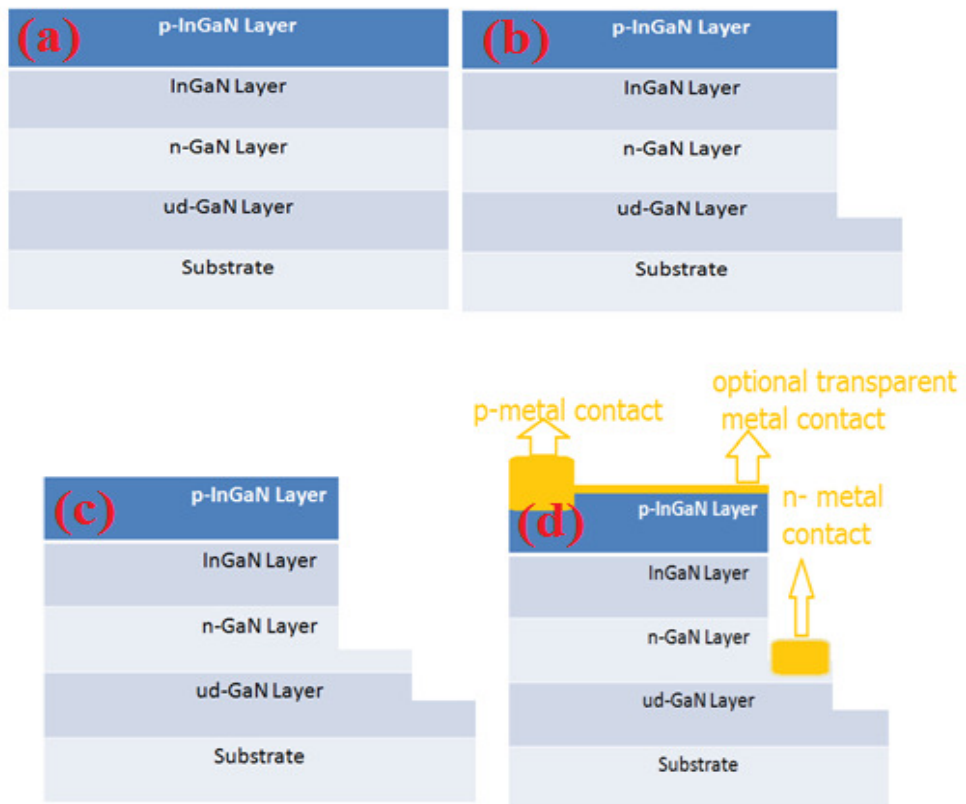


Figure 5.7. Typical device fabrication sequence: (a) cross section of solar cell structure, (b) device isolation, (c) mesa etching and (d) metal depositions.

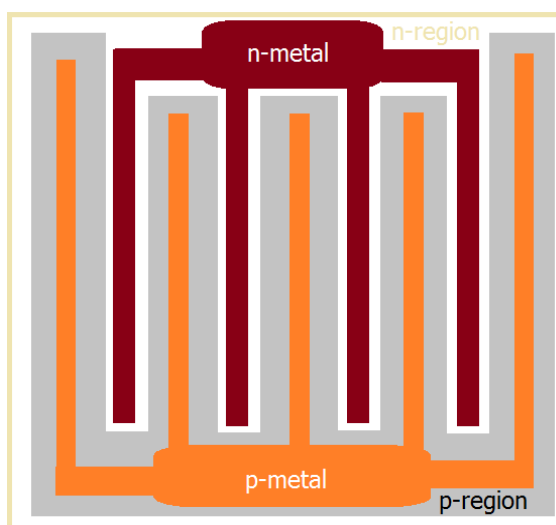


Figure 5.8. Top-view image of the fabricated solar cell devices.

CHAPTER 6

RESULTS AND DISCUSSION

In the preceding chapters, the growth of In rich InGaN epitaxial layers and fabrication of InGaN solar cells were presented. Those epitaxial structures were grown on sapphire substrates using a MOCVD system.

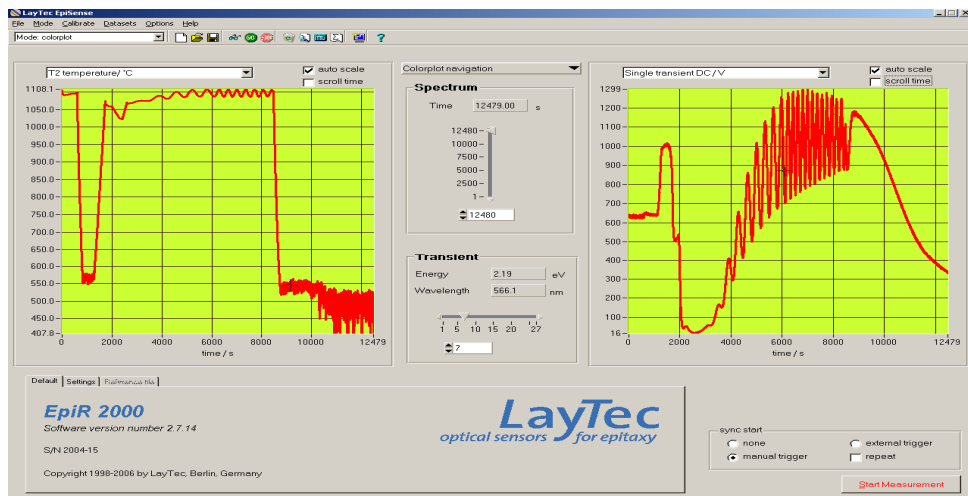
6.1. Characterization of In rich InGaN epilayers

In this part of the thesis, structural and optoelectronic characterization results of the In rich InGaN layer is presented.

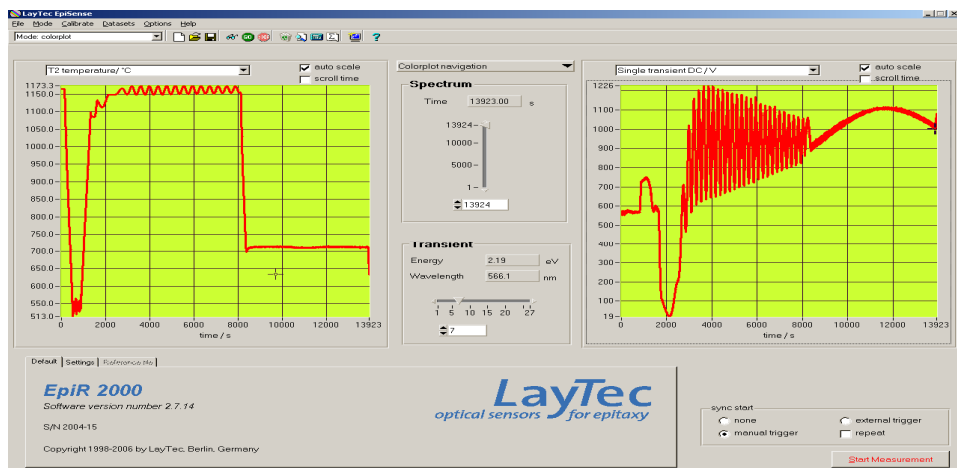
6.1.1. In-situ Characterization

This kind of characterization was performed during material growth, so it is possible to make changes on the growth during ongoing processes.

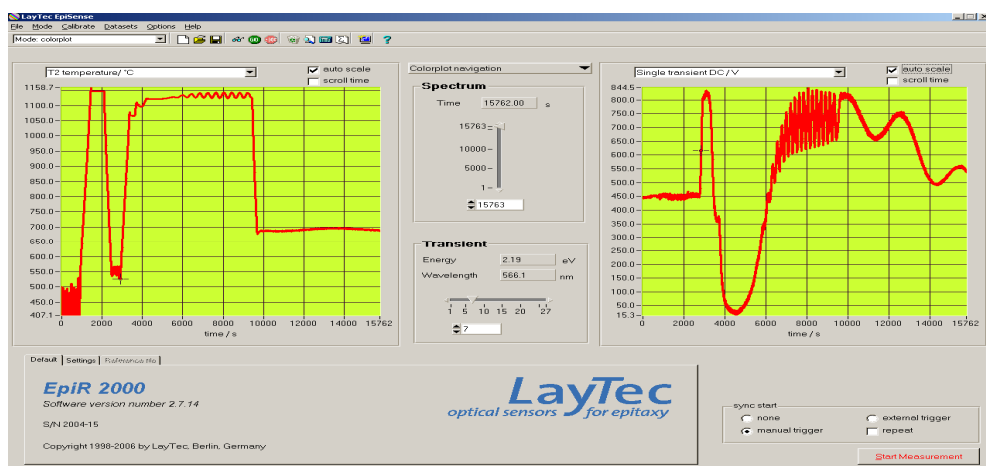
LayTec in-situ monitoring equipment was used to optimize the surface temperature, growth rate and film thickness. It also provides additional information on the surface roughness of the growing thin film. Reflectance measurements of InN and InGaN epilayers with various In contents are shown in Figure 6.1.



a



b



c

Figure 6.1. LayTec Reflectance of growing (a) InN, (b) In_{0.93}GaN and (c) In_{0.06}GaN.

LayTec reflectance measurements show that all GaN buffer layers have very similar layer thicknesses. When the InGaN part of the reflectance measurement was considered, it was found that the period of reflectance oscillation decreased at high growth rates. This signifies that the growth rate increases with decreasing In content in InGaN epilayers.

6.1.2. XRD Measurements

All InGaN alloy layers were characterized by Rigaku Smartlab X-Ray diffractometer. The X-Ray tube used in this experiments has a Cu anode ($K_{\alpha}=1.544$ Å) where the maximum power was 3 kW. Figure 6.2 shows the (ω - 2Θ scan) X-Ray spectra of InGaN layers grown on an identical GaN template, in which In composition is changing from 20 to 100%. (JCPDS Card No: 2-1078 for GaN and 2-3450 for InN, respectively).

Crystal failures are arising from point defects like Ga/N vacancies, antisites and unintentional doping (C, H or O which are always present in growth atmosphere). Point defects are also generated because of the difference in crystal constant of substrate and growing material. Diffusion of the point defects may lead to stacking faults and dislocations which effects crystal quality. On the other hand most of the defects in III- nitrides act as a donor states which give extra electron to the structure. High dislocation density also triggers the electron concentration in the structure which have great effect on device performances.

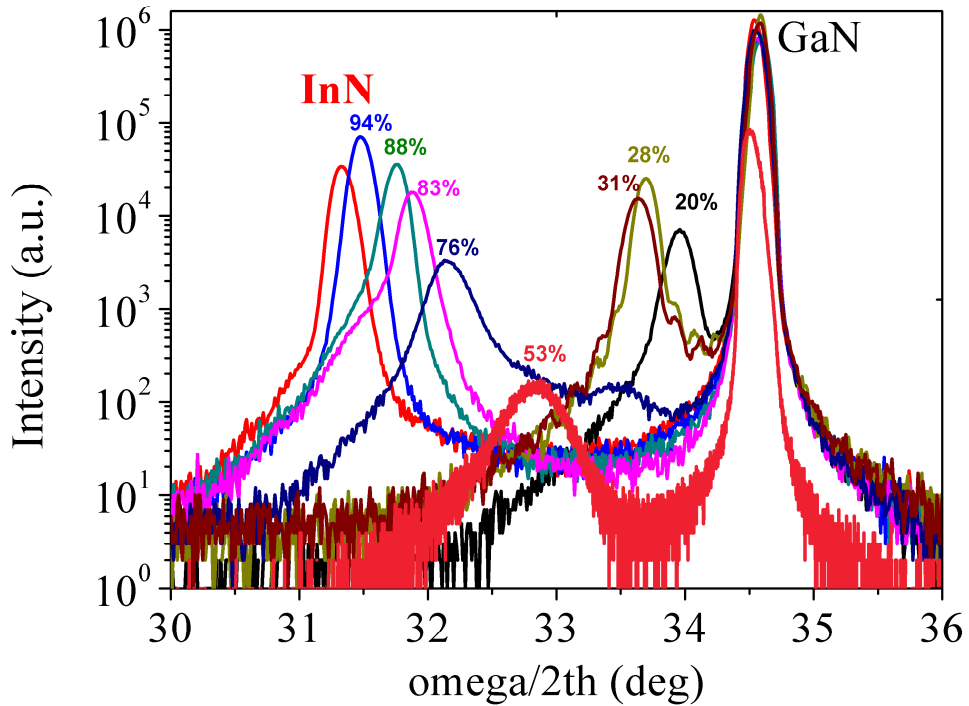


Figure 6.2. X-Ray spectra of $\text{In}_x\text{Ga}_{1-x}\text{N}$ layers ($x = 0.2:1.0$).

In composition in InGaN epitaxial layers were calculated by Vegard's law;

$$c_0(x) = c_1(\text{InN}) + (1 - x) c_2(\text{GaN}) \quad (5.2.)$$

, where c_1 and c_2 are the crystal constants of InN and GaN, respectively. This calculation were carried out assuming the InGaN epilayers are fully relaxed since the thickness of all epilayers were greater than 75 nm^[71].

The crystal quality of InGaN alloys was characterized through XRD measurements. Full width at half maximum (FWHM) values for (002) peak are shown in Figure 6.3 with respect to In composition. Only In 0.53 GaN layer was found to be a FWHM value of 1750 arcsec, whereas FWHM value for all the other compositions were found to be lower than 1200 arcsec. Bin Liu^[48], B.N. Pantha^[49] and M.Horie^[50] have reported similar or even worse FWHM values, which mean that the crystal

quality of the InGaN epilayers we obtained with different contents, were better than those in literature.

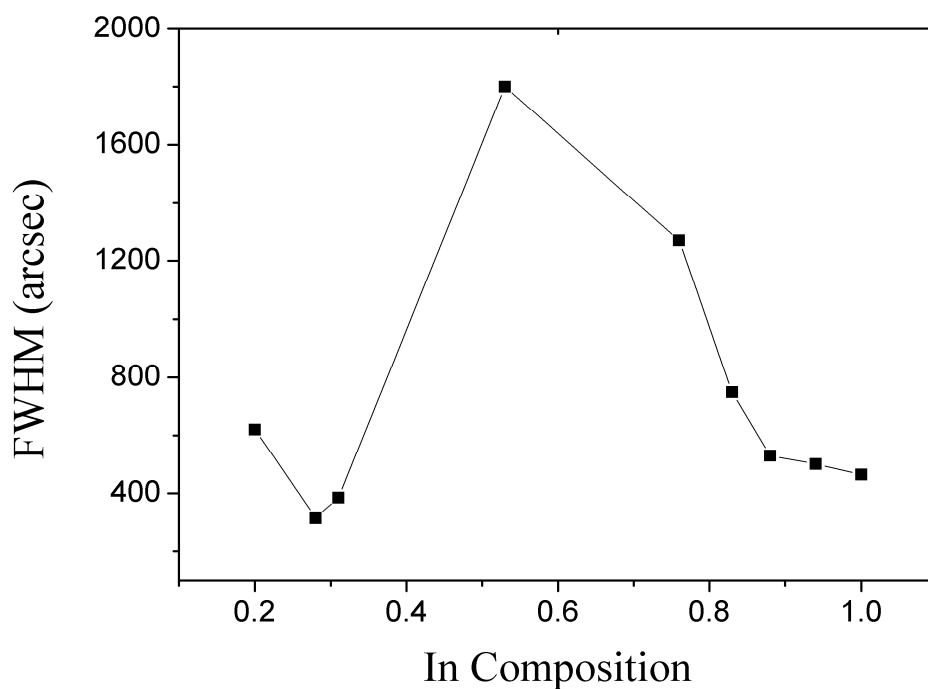


Figure 6.3. XRD FWHM values of $\text{In}_x\text{Ga}_{1-x}\text{N}$ layers ($x=0.2:1.0$). Lines are for visual aid.

Instrumental broadening which arises from unresolved α_1 and α_2 , non-monochromaticity of the source and imperfect focusing was determined by measuring the calibration sample (AlN buffer on c-plane sapphire substrate). There was observed less than 4% instrumental broadening when compared FWHM values of calibration sample measured at the initialization of the XRD system and 3120 lamp hours after initialization. InGaN epilayers with different In compositions measured at the same batch which means that instrumental broadening has less effects on measurement results.

6.1.3. Atomic Force Microscopy (AFM) Measurements

The degradation of material quality appears to be correlated to a change of In composition in InGaN epitaxial structures. Figure 6.4 shows the AFM images of InGaN layers with different In compositions. The temperature was decreased to enhance In incorporation, which deteriorates the epitaxial film quality. A gradual change of growth mode from step-flow growth Figure 6.4 (a) to two-dimensional island growth (Figure 6.4 (c)) was observed due to the lower adatom surface mobility at lower growth temperatures. Lowering adatom surface mobility cause an increase in the surface roughness. Similar effect of growth temperature on growth modes was observed by Young Huang ^[55].

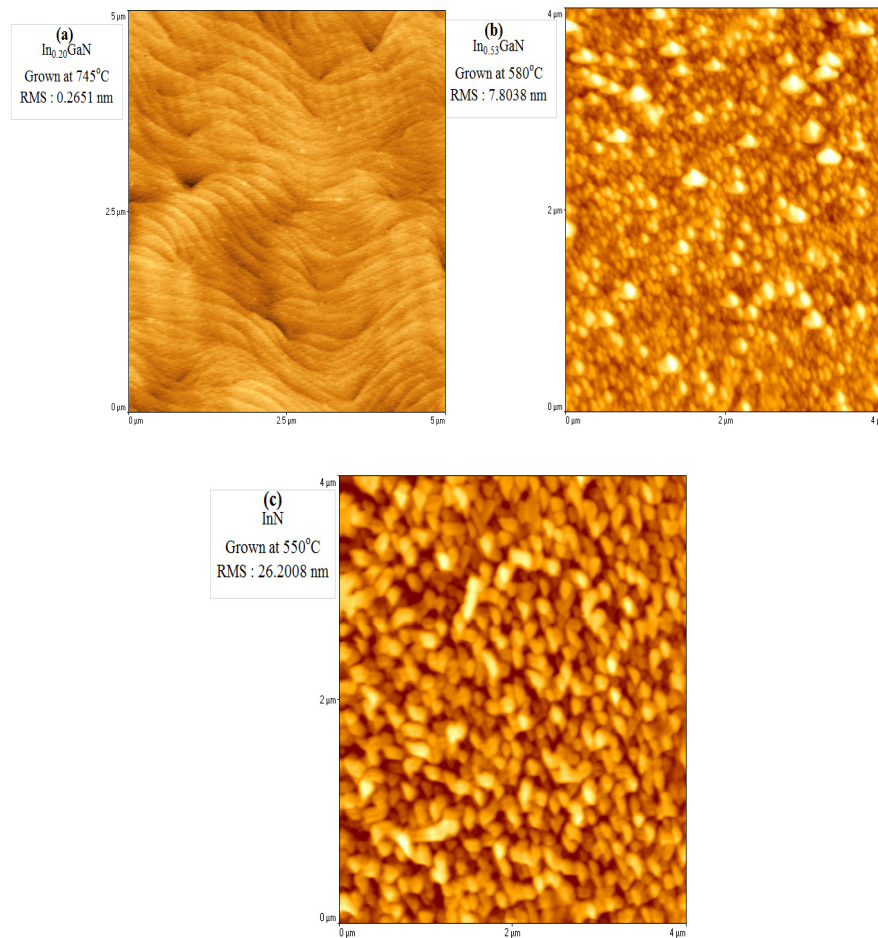


Figure 6.4. AFM images of the $\text{In}_x\text{Ga}_{1-x}\text{N}$ layers with (a) $x=0.20$, (b) $x=0.53$ and (c) $x=1.00$.

6.1.4. Hall-Effect Measurements

All InGaN alloy layers were characterized through ECOPIA HMS-3000 Hall Effect Measurement system, where the magnetic field strength was 0.57 Tesla. Measurements showed that InGaN layers have high background electron concentrations ($< 10^{19} \text{ cm}^{-3}$) even without doping. High background electron concentrations caused a decrease in mobility. Room-temperature electron mobility (μ) and electron concentration (N_b) were obtained from Hall-Effect measurements. Background electron concentration and mobility of InN was found to be around $4 \times 10^{19} \text{ cm}^{-3}$ and $270 \text{ cm}^2/\text{V.s}$, respectively. Similar values have been reported by B.N. Pantha^[53] and V.Lebedev^[51]. All InN layers grown using MOVCD system showed high electron concentration, which clearly presents a drawback for device applications. High background electron concentration arises from H and O impurities, nitrogen vacancies (lower decomposition of NH_3 at InN growth temperatures, which were about 700°C and lower than GaN growth temperatures which were about 1000°C) and In vacancy/N antisite. The background electron concentration (shown in Figure 6.5(a)) was $\sim 10^{19} \text{ cm}^{-3}$ for $\text{In}_{0.2}\text{Ga}_{0.8}\text{N}$ and found to increase almost linearly with In content. InN has the highest background electron concentration, which was $> \sim 10^{20} \text{ cm}^{-3}$ as shown Figure 6.5 (a). Electron mobility showed a similar behavior with FWHM values (Figure 6.2.) with increasing In content in InGaN layers. Change in mobility and FWHM values clearly present deterioration of the crystal quality within InGaN epitaxial structures at intermediate values.

Decreased In content in InGaN layers also decrease the background electron concentration.

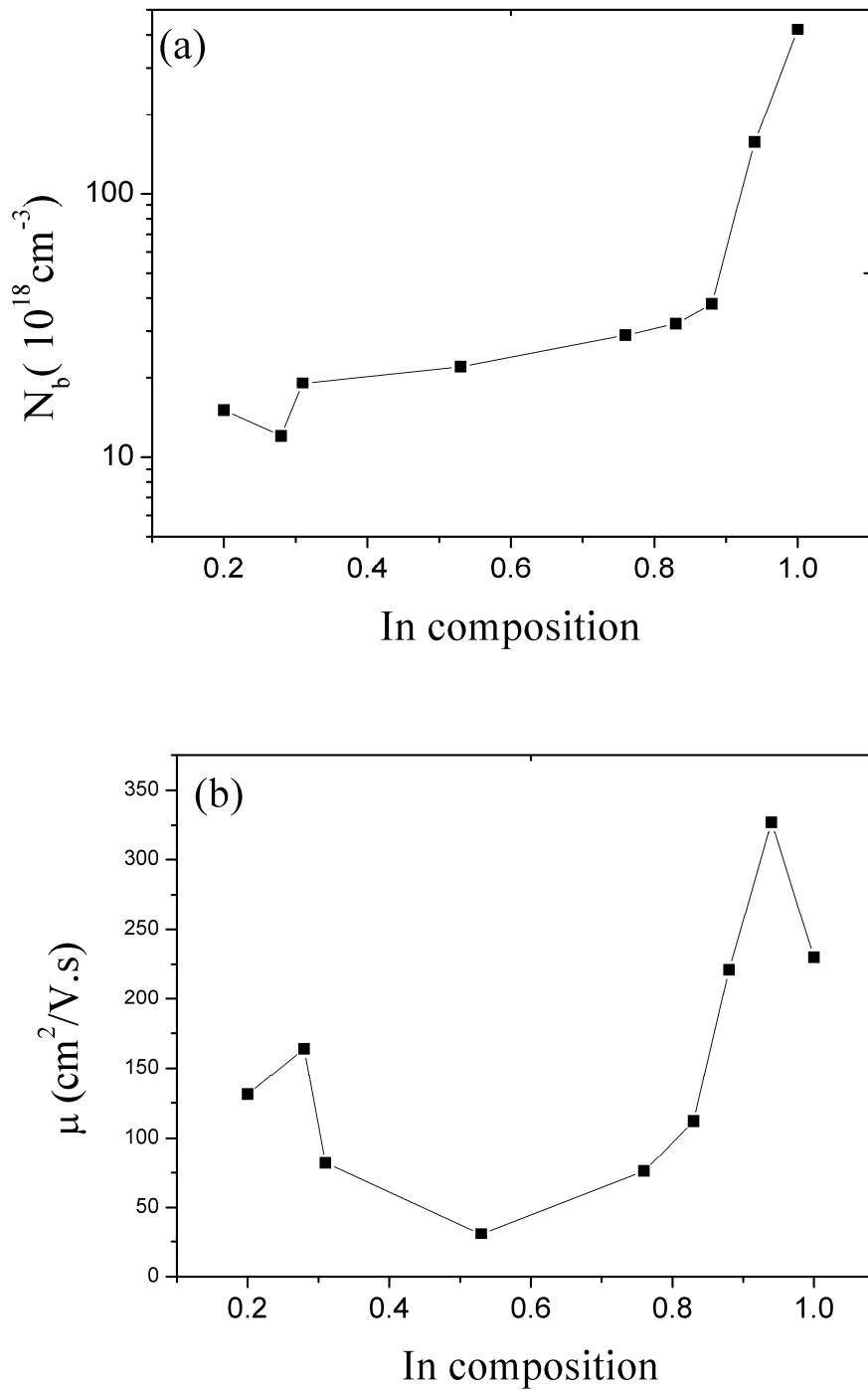


Figure 6.5. (a) Background electron concentration (N_b) and (b) mobility (μ) of InGaN epitaxial layers with different In composition. Lines are for visual aid.

6.1.5. Absorption Measurements

Absorption measurements of InGaN epilayers with different In composition revealed that absorbance increases with In content. The bandgap of the InGaN epitaxial structure decreases with increasing In content, which enhances absorption. Figure 6.6 (a) and (b) shows the combined transmission with reflection and absorption spectra of the InGaN epitaxial structure with different In compositions, respectively.

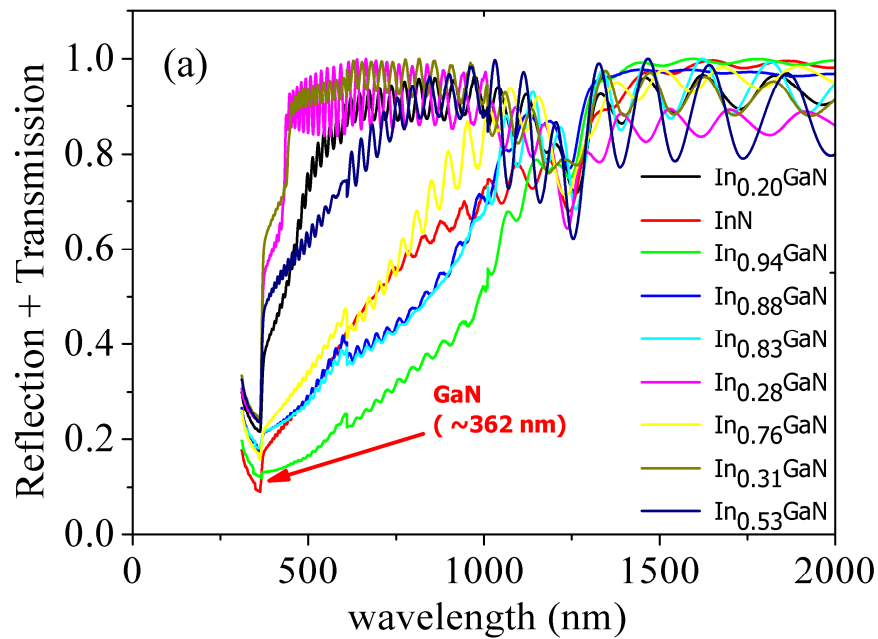


Figure 6.6. (a) Combined Reflection with transmission and (b) absorption spectra of the InGaN layers with different In compositions.

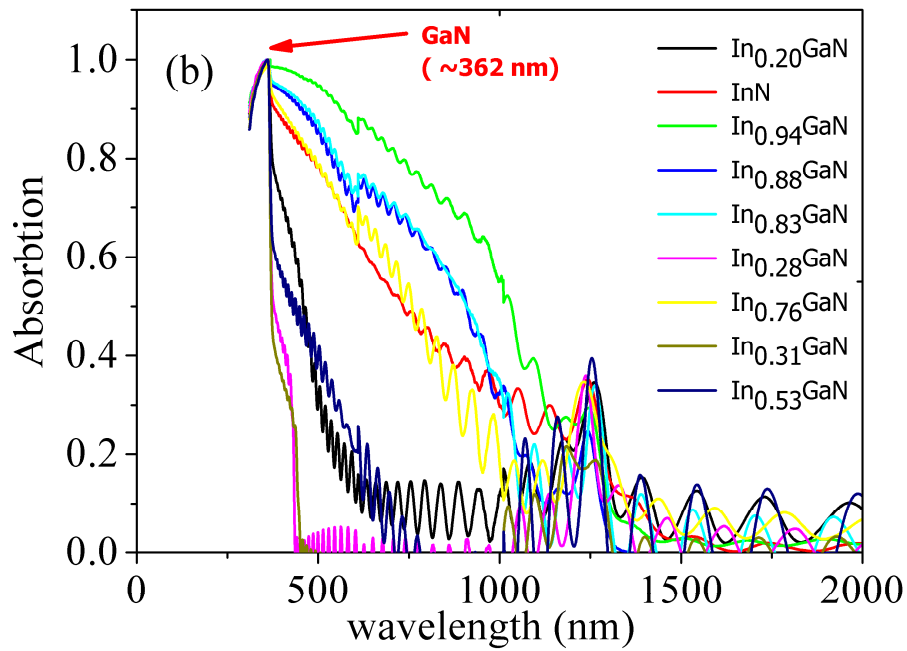


Figure 6.6. (a) Combined Reflection with transmission and (b) absorption spectra of the InGaN layers with different In compositions (continued).

The absorption edge energy or optical band gap was determined using Tauc plot, briefly extrapolating the linear part of the squared absorption multiplied by energy (αE)² versus energy (E) for a direct band gap semiconductors. E is the energy of the incident photons. Tauc plots for InGaN epitaxial structures with different In compositions are given in Figure 6.7. Band gaps are clearly marked on the figure.

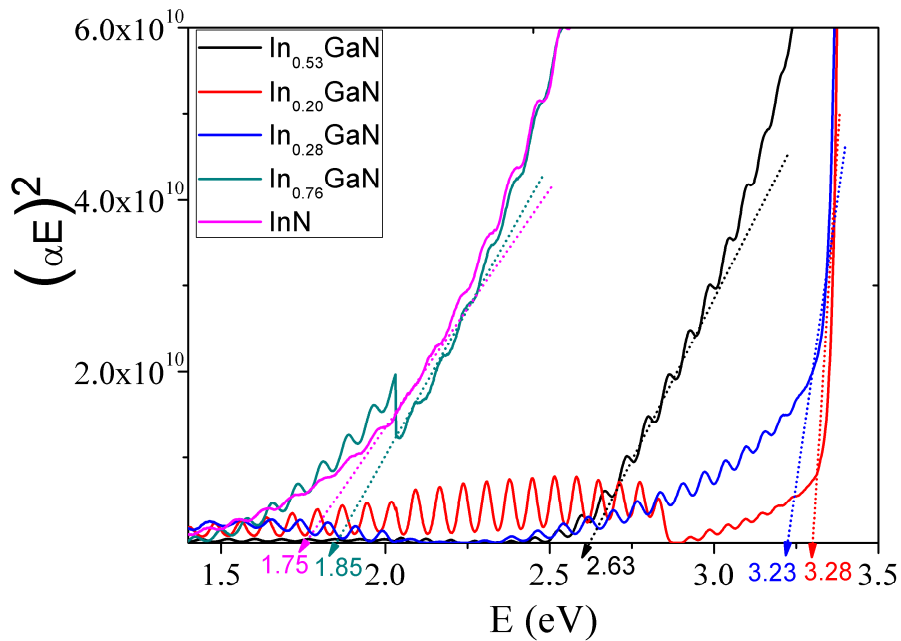


Figure 6.7. Tauc plot of InGaN epitaxial structures with different In composition.

The bandgap of the InN epitaxial structure was found to be 1.75 eV which is a lot higher than that of the previously reported values of 0.7eV ^[16]. In spite of the reported lower band gap values for InN there is still a debate about the band gap of InN. There are various band gap values were reported for the band gap of InN which are changing from 0.7 eV to 1.9 eV ^[68]. The band gap of InN epitaxial structures not only depends on growth techniques (RF Sputter, MBE, MOCVD or etc.) but also depends on the carrier concentration. In nominally doped semiconductors the Fermi level lies above the donor states, more and more donor states produced by increasing the doping concentration which pushes Fermi level to a higher energy level or even in to conduction band. This effect is called to Burstein-Moss shift.

$$E_g = 0.65 \text{ eV} + 0.0116 (m_0/m^*) \times (n \times 10^{-19})^{2/3} \text{ eV} \quad [69][70] \quad (5.2.)$$

, where m^* is the free electron effective mass which also depends on the electron concentration, m_0 is the mass of electron in vacuum and n is the electron concentration.

A strong Burstein-Moss shift of the absorption edge was observed due to the high carrier concentration ^[57]. According to the Eq. 5.1, if the carrier concentration exceeds $3 \times 10^{20} \text{ cm}^{-3}$ then there is an additional 1eV comes from the additional terms shown in the Eq 5.1.

InGaN epitaxial structures yielded slightly higher absorption edge as well, but the Burstein-Moss shift was lower since the carrier concentration of InGaN epitaxial structures was lower than that of InN.

6.2. InGaN Solar Cell Characterization

6.2.1. Material Characterization for Solar Cell Structures

Structural analysis of preliminary growths (ud-GaN, n-GaN and p-InGaN) were done by HR-XRD measurements. Electrical characterizations of those structures were also done by Hall measurements following the deposition of suitable metal contact pads. Figure 6.8 shows the XRD spectrum of p-In_{0.07} GaN. The figure shows both the crystal quality and In content of InGaN epilayer, which was designed to be used as p-region in InGaN solar cell structures. (JCPDS Card No: 25-1133 for AlN, 2-1078 for GaN and 2-3450 for InN).

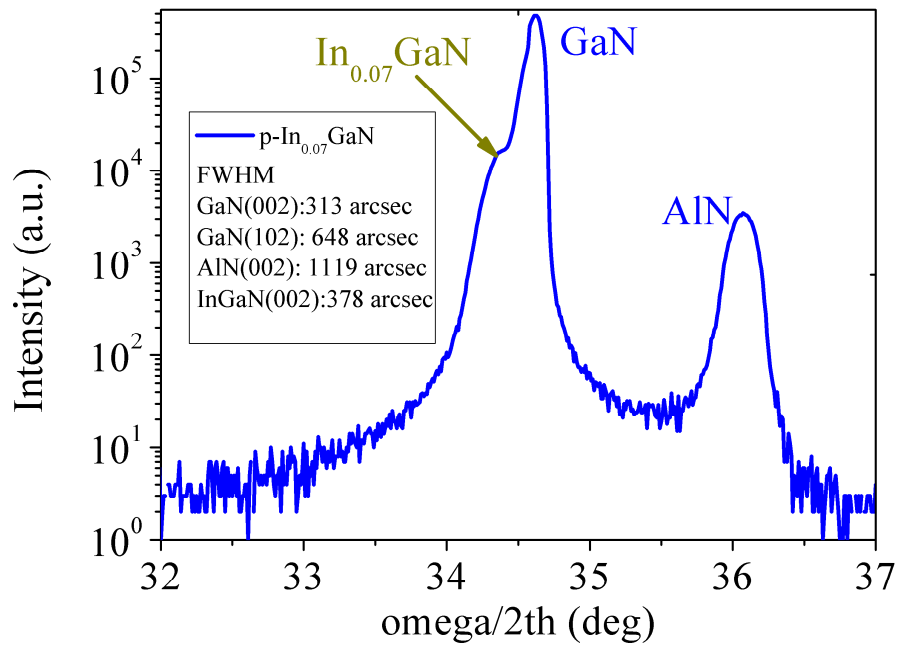


Figure 6.8. XRD spectrum of p- $In_{0.07}GaN$.

Table 6.1 shows the comparison of the obtained experimental data to those in literature. Characterizations of individual layers that are intended to be used in the solar cell structure showed reasonable quality. GaN layers, in particular, revealed better electrical and structural characteristics compared to those in literature.

Table 6.1. Comparison of the fabricated thin films and similar thin films from literature

| | | ud-GaN | n-GaN | p-In _{0,07} GaN |
|-----------------------|---------------------------------------------------------------------------------------|--------------------------------------------------------|----------------------------------------------|------------------------------------|
| Experimental Data | Hall Measurements N _s (cm ⁻³) / μ (cm ² /V.s) | 1.6x10 ¹⁶ /430 | 2.0x10 ¹⁸ /267 | 2.1x10 ¹⁸ /5.5 |
| | XRD Measurements (arcsec) | GaN(002): 306 GaN(102): 302 | GaN(002): 270 GaN(102): 342 | InGaN(002): 378 |
| Literature Comparison | Hall Measurements N _s (cm ⁻³) / μ (cm ² /V.s) | 1-3x10 ¹⁷ / 80-160 [58] | 1.1x10 ¹⁸ / 379 [59] | 1.1x10 ¹⁸ / 1.2 [59] |
| | XRD Measurements | GaN(002): 350- 450 GaN(102): 500- 900 [58] | GaN(002): ~600 GaN(102): ~1600 [61] | InGaN(002): 400-1000 [60] |

The Figure 6.9 shows the XRD patterns of the fabricated InGaN solar cell structures. Widening in InGaN peaks is an evidence of grading in the InGaN layer within the structure. The grading in the InGaN layer was such that there is high In content at the beginning and In percentage gradually decreases down to 6-7%. This value is almost equal to the In content of p-InGaN layers located on top of the solar cell structures. For solar cell structures, three different samples were grown on sapphire substrates, where In contents were changing gradually from 9% (Sample A), 16% (Sample B) and 30% (Sample C).

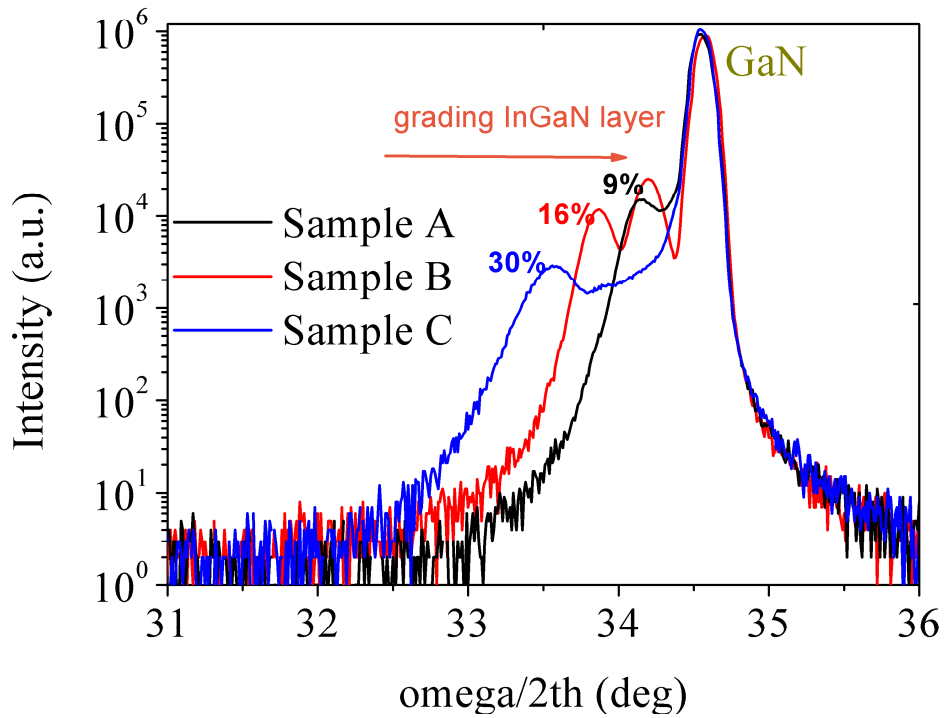


Figure 6.9. XRD spectra of the fabricated solar cell structures.

6.2.2. Absorption Measurement of Solar Cell Structures

Combined transmission with reflection and absorption spectrum of InGaN solar cell structures are shown in the Figure 6.10 (a) and (b), respectively. It is seen that absorption increases with In content. This is because of the decrease in bandgap with increasing In content, which increases the number of captured photons that are captured.

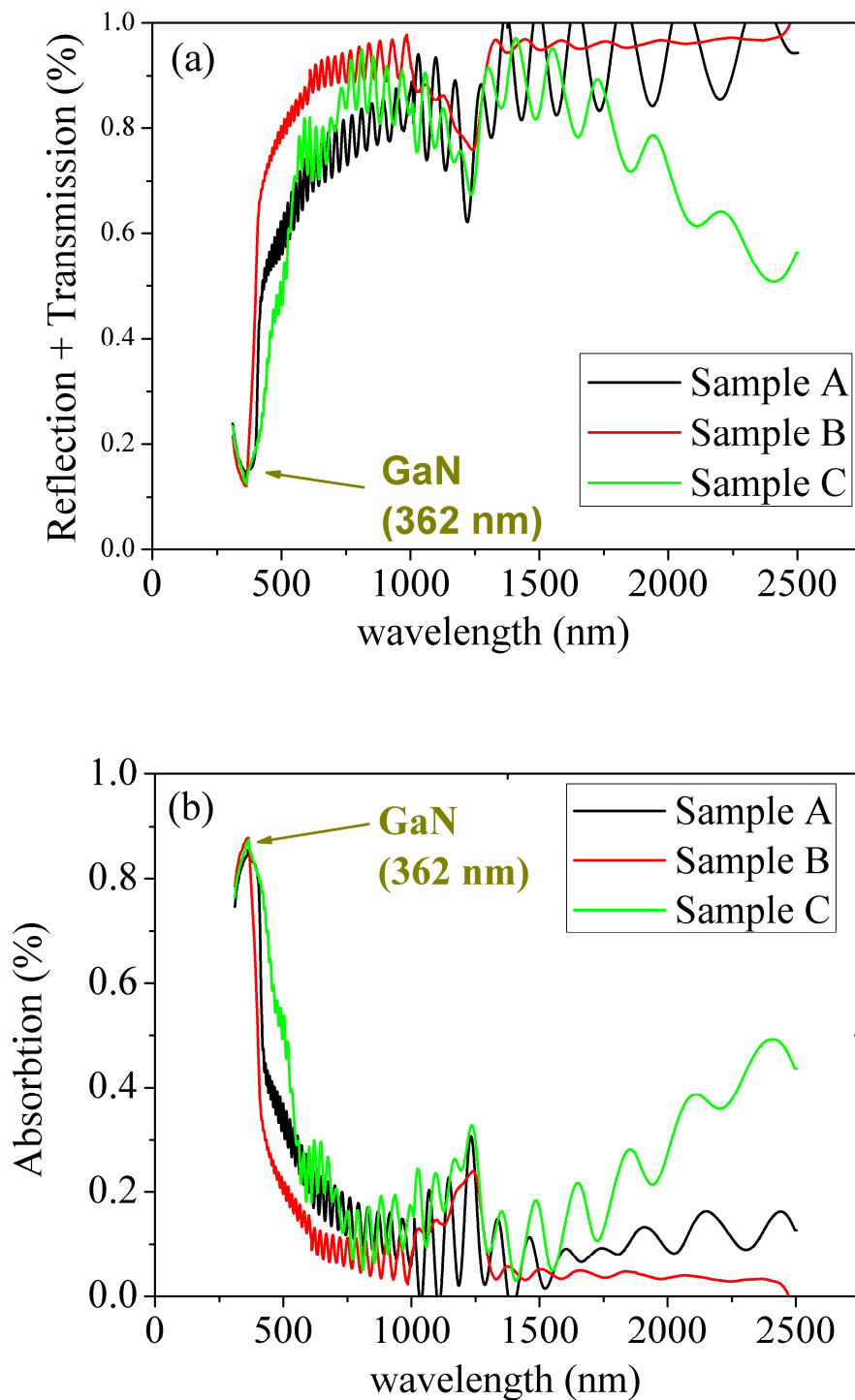


Figure 6.10. (a) Combined reflection with transmission and (b) absorption spectra of the InGaN solar cell structures with different In compositions.

6.2.3. Current Density Voltage (J-V) Characteristics

Electrical performance of the solar cells could be determined by current density versus voltage (J-V) measurements. J-V characteristics of fabricated solar cells were measured by a semiconductor device analyzer (Agilent Technologies, B1500 A) under a standar solar simulator with one-sun air mass (AM) 1.5 global light source ($100\text{mW}/\text{cm}^2$) at room temperature.

J-V characteristic of the fabricated InGaN solar cells structures under dark and illuminated conditions with different In composition are shown in Figure 6.11. (a)- (c). The area of the fabricated solar cell were 1mm^2 including metal contact pads.

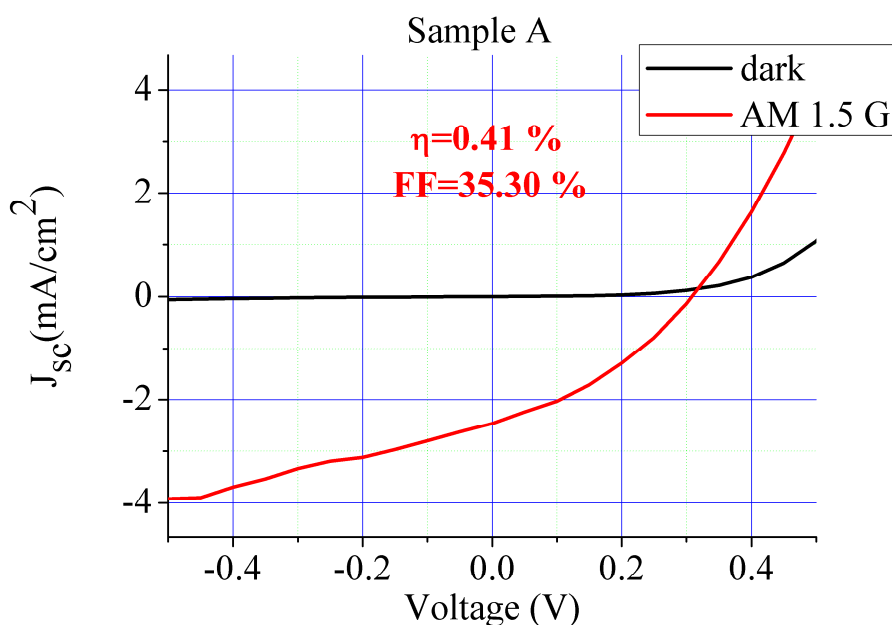


Figure 6.11. J-V characteristics of the fabricated solar cells with different graded In compositions of (a) 9%, (b) 16%, (c) 30% .

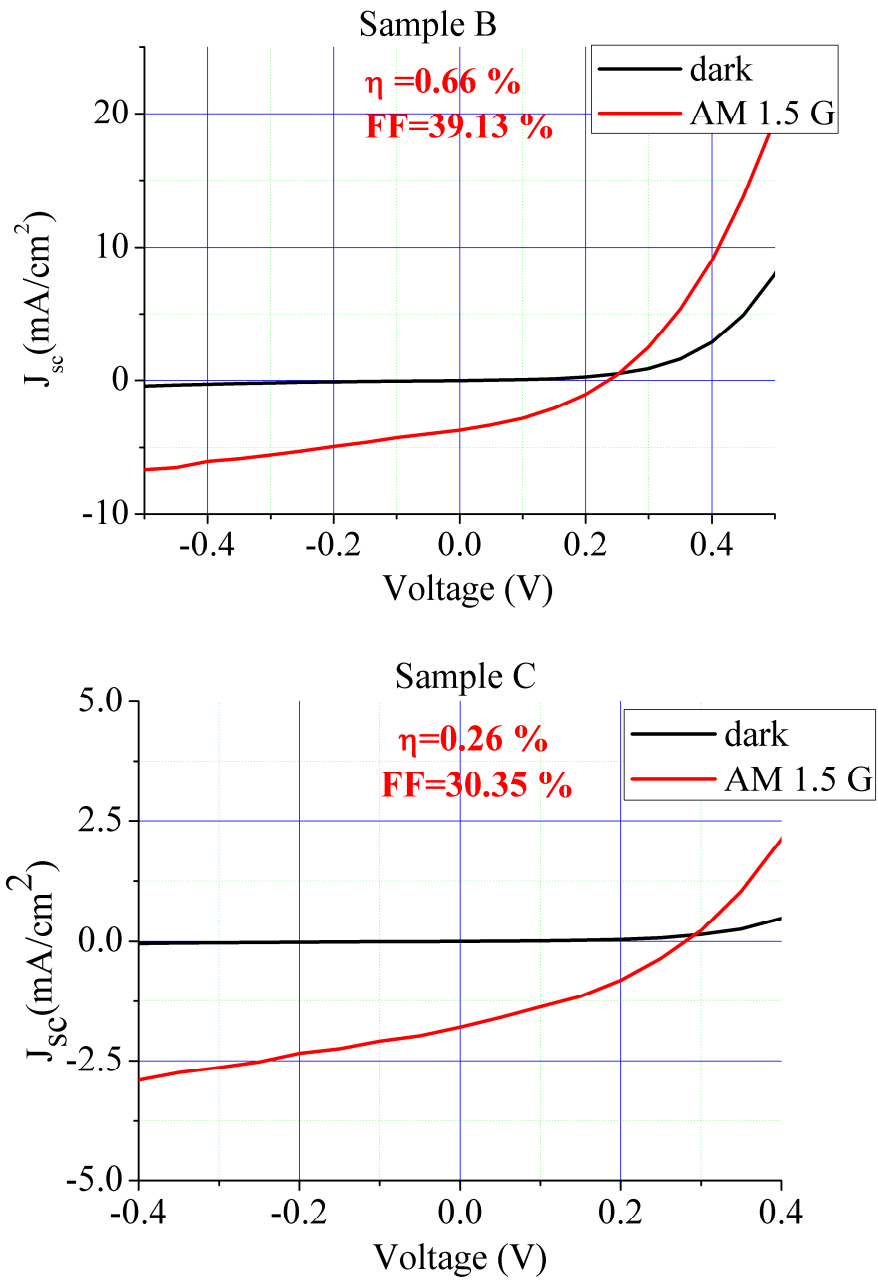


Figure 6.11. J-V characteristics of the fabricated solar cells with different graded In compositions of (a) 9%, (b) 16%, (c) 30% (continued).

From J-V characteristics, solar cell parameters such as FF, R_s , R_{sh} and η were calculated and tabulated in Table 6.2.

Table 6.2. Solar cell parameters.

| Sample Code | In composition (%) | n (ideality factor) | FF (%) | R_s (Ω) | R_{sh} (Ω) | η (%) |
|-------------|--------------------|---------------------|--------|--------------------|-----------------------|------------|
| Sample A | 9 | 8.94 | 35.30 | 227 | 4.9×10^3 | 0.41 |
| Sample B | 16 | 10.21 | 39.13 | 136 | 9.1×10^2 | 0.66 |
| Sample C | 30 | 9.56 | 30.35 | 74 | 7.3×10^3 | 0.26 |

The ideality factor is governed by resistivity, carrier transport and recombination which are used to evaluate the materials quality on device performance. Ideality factor of fabricated solar cells was higher than its typical values of 1-2. Abnormally high diode ideality factors may be summation of a series of ideality factors. Shah^[62] et al. reported high ideality factor of a p-n junction diode. Measured high ideality factor of the p-n junction was attributed to the summation of ideality factors of the individual junctions. The magnitude of ideality factor also depends on carrier transport mechanism. The dominant mechanism for carrier transport is tunneling in the case of the high carrier concentration within the epitaxial structures which results in high ideality factors. K.Mayes^[73] and Lei Wang^[72] have already reported GaN based diode structures with high ideality factor which were attributed to carrier transport mechanism arising from high carrier concentration.

The V_{oc} 's for the fabricated solar cells are typically 0.4 eV less than the bandgap of the material. The V_{oc} values of fabricated solar cells depend on both In composition^[63] and Shockley-Read-Hall recombination, which arises from mid-gap states.

Increasing In content in InGaN solar cells decreases V_{oc} values [63]. Crystal imperfections (dislocations, vacancies, etc.) increase mid-gap states, which is also decreasing V_{oc} . Lowering growth temperature in order to increase In composition also increase defect density within InGaN epitaxial materials. Defects, like O, H are always in growth atmosphere and anti-sited atoms and vacancies are also present which deteriorates crystal quality. On the other hand decreasing growth temperature increases N-vacancies since the decomposition rate of NH_3 is lower. These N-vacancies introduces mid-gap states which decrease V_{oc} 's of fabricated solar cells.

Large series resistance (R_s) was due to metal-semiconductor interfaces, non-optimized metal contacts and graded profile of the active layer, which led to the formation of additional interfaces in the active region. Graded solar cell structure introduces number of interfaces which increase overall bulk resistance of the material. One of the main reason which increase the R_s is solar cells is the un-optimized metal contacts for p-type materials. In this study Ni/Au alloys were used but in order to decrease R_s values in solar cells more efforts needed to optimize proper metal alloys for p-type materials. Similar results were reported by Liwen Sang et al [64].

The R_{sh} depends on both bulk resistances of the semiconductor and microfabrication processes. Lower R_{sh} arises due to the presence of dislocations in InGaN epitaxial structure and absence of a passivation layer within the InGaN solar cells.

The fabricated InGaN solar cells yielded low FF, which is a function of V_{oc} . High carrier concentration introduces mid-gap states which decrease V_{oc} of fabricaqtged solar cells. Not only V_{oc} but also other factors can affect FF, such as parasitic resistance, doping level, recombination, etc. High number of defects induced by degraded crystalline quality of InGaN epitaxial structure enhances recombination. In addition, large series resistance also results in low FF [65].

It was observed that the current density (J_{sc}), and hence, efficiency (η) increased with increasing In content in the active layer of solar cells, but at some point a decrease in both J_{sc} and η was observed with a further increase in In composition. This is due to the increase in electron concentration (decreasing mobility) and deterioration of epilayer crystal quality.

CHAPTER 7

CONCLUSIONS

In the preceding chapters, the growth details of high quality InGaN epilayers with different In composition and consequent fabrication details of InGaN based solar cell structures by MOCVD system was presented. Following that microfabrication processes was presented shortly. Performance of InGaN based solar cell devices was also discussed.

In the first part, InGaN epilayers were grown on c-plane sapphire substrates. XRD measurements revealed that In contents in InGaN epitaxial structures were varied from 20 to 100% (InN) with high crystal quality. There were observed deterioration in crystal quality at middle In composition. Dominant crystal matrices were InN and GaN for higher and lower In composition, respectively. At middle In composition atomic disorder might be higher because of the absence of dominant crystal matrix which could result in crystal failure.

AFM characterization showed that growth mode of InGaN epitaxial structures changed from 2D to 3D growth. The reason in change of growth mode was attributed to lower adatom surface mobility when decreasing growth temperatures.

Room temperature Hall effect measurements revealed an increase in the background electron concentration with increasing In content due to vacancies and dislocations in InGaN epitaxial structure. N-vanancies are the one of the main reason for high carrier concentration in InGaN epitaxial structures because of the lower decomposition rate of NH_3 at InGaN growth temperatures.

Room temperature reflection and transmission measurements revealed that absorption of InGaN epitaxial structures increases with In content. It was also found that absorbance increases with In content. The absorption edge energy or optical band gap was determined using Tauc plot. A strong Burstein-Moss shift of the absorption edge was observed due to the high carrier concentration. Calculation of optical band gap from carrier concentration also revealed that, if the carrier concentration exceeds $3 \times 10^{20} \text{ cm}^{-3}$ then there is an additional 1eV comes.

In the second part, InGaN solar cell structures with different In compositions in active region (Sample A, Sample B and Sample C) were successfully grown on c-plane sapphire substrates. Characterization measurements confirmed the increasing In composition in active layer. Solar cells were characterized following standard microfabrication processes which include multiple photolithography, etching, metal depositing and annealing.

Increase in the In content in active region of solar cells improved efficiency; but, further increase in In content within the active layer deteriorated efficiency. This is because of the decreased crystal quality and increased background electron concentration with increasing In content within the active layer of solar cells.

CHAPTER 8

FUTURE DIRECTIONS

To further characterize the fabricated InGaN solar cells, external quantum efficiency (EQE) and incident photon to current efficiency (ICPE) measurements will be performed and a comprehensive investigation on measurement result will be done.

To further increase the photovoltaic conversion efficiency, both the electron concentration and the defect density of In rich InGaN epitaxial structures needs to be decreased. Since background electron concentration is increasing with N-vacancies (lack of available N at lower temperature), a suitable hydride source that efficiently decompose at lower growth temperatures in order to grow InGaN epitaxial structures efficiently. Another approach could be doping of InGaN epilayers to decrease the electron concentration; but, this will also deteriorate the crystal quality and interfacial roughness.

For future work, one might think of suppressing the electron concentration by adjusting growth parameters, while keeping a reasonable crystal quality for solar cell applications. By this way, it might be possible to shrink the gap between theoretical and experimental performance of InGaN solar cells.

LIST OF REFERENCES

- [1] Jennifer Jo Krohn, Exploration of Graded Indium Gallium Nitride Heterojunction Solar Cells For Laterally Integrated, Spectrally-Split Solar Cell Arrays, MSc, Faculty of Graduate School of The University of Minnesota, 2011
- [2] World Carbon Dioxide Emission, <http://www.docstoc.com/docs/9885555/World-carbon-dioxide-emissions-from-fossil-fuels-1900-1999-and>
- [3] Jessica Christine Lai, The use of nanostructured calcium silicate in solar cell, MSc Thesis, School of Chemical and Physical Sciences, 2009, Victoria University of Wellington
- [4] Basic Research Needs for Solar Energy Utilization: Report of the Basic Energy Sciences Workshop on Solar Energy Utilization' April 18 – 21 2005, <http://chem.ps.uci.edu/~lawm/DOE%20Solar%20Pathways%20Report.pdf> (Retrieved August 15, 2011)
- [5] Renewables 2011 Global Status Report, www.ren21.net (Retrieved August 14, 2011)
- [6] U.S. Department of Energy, The History of Solar. <http://www1.eere.energy.gov>. (Retrieved July 22, 2011)
- [7] Oliver Morton, Solar Energy: A new day dawning?, Silicon Valley sunrise, Nature 443, 19-22, doi: 10.1038/443019a, 2006
- [8] Environmental Defense Fund, <http://www.edf.org>. (Retrieved August 8, 2011)
- [9] Richard Williams, Becquerel Photovoltaic Effect in Binary Compounds J. Chem. Phys. 32, 1505, 1960
- [10] Perlin, From Space to Earth (The Story of Solar Electricity). Harvard University Press (1999)

- [11] Acetal-Lucent, <http://www.alcatel-lucent.com/wps/portal/belllabs>.
(Retrieved August 8, 2011)
- [12] Shah et al, Photovoltaic Technology: The case for thin-film solar cell, *Science*, 285, 692 (1999)
- [13] William Shockley et al, Detailed Balance Limit of Efficiency of p-n Junction Solar Cells, *J. Appl. Phys.*, 32, 510 (1961).
- [14] Renewable Energy Focus, www.renewableenergyfocus.com
(Retrieved August 12, 2011)
- [15] U.S. Department of Energy, 1\$/W Photovoltaic Systems, <http://www1.eere.energy.gov>.
(Retrieved August 16, 2011)
- [16] National Renewable Energy Laboratory.
<http://rredc.nrel.gov/solar/spectra/am1.5/>.
(Retrieved May 2, 2011)
- [17] Junqiao Wu et al, When group-III nitrides go infrared: New properties and perspectives, *J. Appl. Phys.*, 106, 011101 (2009).
- [18] J. Wu et al, Band gaps of InN and group III nitride alloys, *Superlattices and Microstructures*, 34, 63-75 (2003)
- [19] A. Devos, *Endoreversible Thermodynamics of Solar Energy Conversion*, Oxford University Press, New York (1992).
- [20] W.Walukiewicz et al, Optical properties and electronic structure of InN and In-rich group III-nitride alloys, *Journal of Crystal Growth* 269 (2004) 119–127
- [21] B. Monemar et al, III-V nitrides-important future electronic materials, *Journal of Materials Science: Materials in Electronics* 10(1999) 227-254
- [22] E.T. Yu, M.O. Manasreh, *III-V Nitride Semiconductors Applications and Devices*, Vol.16
- [23] S. Strite and H. Morkoc, GaN AlN and InN: A review, *J. Vac. Sci. Technol.* 1992 B 10(4)
- [24] S. N. Mohammad and H. Morkoc, *Prog. Quant. Electr.* 1996 20(5/6) pp. 361-525.
- [25] Hadis Morkoç, *Handbook of Nitride Semiconductors and Devices, Vol.1: Materials Properties, Physics and Growth*

- [26] Ugo Lafont et al, Increasing the reliability of solid state lighting system via self-healing approaches: A review, *Microelectronic Reliability* 52(2012) 71-89
- [27] Chito E. Kendrick, Revisiting Nitride Semiconductors: Epilayers, p-type Doping and Nanowires, Doctor of Philosophy, University of Canterbury, New Zealand, September 2008
- [28] J.M. Olson et al, MOCVD Growth and Characterization of GaP on Si, *Journal of Crystal Growth*, Vol.77, Issue 1-3, p.515-523, 1986
- [29] P.Ruterana, M.Albrecht,J. Neugebauer, ‘Nitride Semiconductors Handbook on Materials and Devices’,
- [30] Zinki Monga, Thermodynamic Studies on the Synthesis of Nitrides and Epitaxial Growth of InGaN, MSc Thesis (2007), University of Central Florida, Orlando, Florida
- [31] Jiun-Yun Li, Material Growth of InGaAs/InAlAs Superlattices for Quantum Cascade Laser Application, MSc Thesis 2007, University of Maryland, Colege Park
- [32] Steven P. DenBaars, Gallium Nitride Materials and Technology, Chapter 3’
- [33] Manijeh Razeghi, The MOCVD Challenge’ Vol2: A survey of GaInAsP-GaAs for photonic and electronic device application
- [34] Stephen Fonash, Solar Cell Device Physics’ Second Edition
- [35] Lewis Fraas, Larry Partain, Solar Cells and Their Applications’ Second Edition
- [36] K.L. Chopra et al, Thin Film Solar Cell: An Overview, *Prog. Photovolt: Res. Apply.* 2004; 12:69-92 (DOI:10.1002/pip.541)
- [37] Martin A. Green, Solar Cell Efficiency Tables (Version 39)’ *Prog. Photovolt:Res. Apply.* 2012; 20:12-20 (DOI:10.1002/pip.2163)
- [38] Omkar K. Jani, Development of Wide-Band Gap InGaN Solar Cells for Himgh-Efficiency Photovoltaics, Doctor of Philosophy, Georgia Institute of Technology, 2008
- [39] Frank Dimroth, High-Efficiency Multijunction Solar Cells, *MRS Bultein*, Volume32, March 2007
- [40] Jerry R. Kukulka et al, Concentrating the Sun, *Photonic Spectra*, 2008

- [41] S.P. Bremner et al, Analysis of Tandem Solar Cell Efficiencies Under AM1.5G Spectrum using Rapid Flux Calculation Method, *Prog. Photovolt: Res. Apply.* 2008; 16:225-233 (DOI:10.1002/pip.799)
- [42] Wu J et al, Unusual properties of the fundamental band gap of InN, *Appl. Phys, Letter.*2002 80 3967
- [43] Balakrishnam R. Jampana et al, Design and Realization of Wide-Band-Gap (~2.67eV) InGaN p-n Junction Solar Cell, *IEEE Electron Device Letter*, Vol.31, No.1, January 2010
- [44] Jenny Hogan, <http://www.newscientist.com/article/dn3145-solar-cells-aiming-for-full-spectrum-efficiency.html>, 2002
- [45] LayTec Information Notes, Version 2, January 2008
- [46] Shunfeng Li, Growth and Characterization of Cubic InGaN and InGaN/GaN Quantum Wells, Doctor of Philosophy, Paderborn University, Germany, 2005
- [47] Ambacher O, Growth and Application of Group III-nitrides, *J.Phys. D: Appl. Phys.* 31 (1998) 2653-2710.
- [48] S. C. Jain et al, Growth and Application of Group III-nitrides, *Journal of Applied Physics* 87, 965 (2000); doi: 10.1063/1.371971
- [49] Brandt O. et al, Improved synthesis of (In,Ga)N/GaN multiple quantum well by plasma-assisted molecular-beam epitaxy, *Appl. Phys. Lett.* 83, 90 (2003)
- [50] Jinn-Kong Sheu et al, Demonstration of GaN-based Solar Cells with GaN/InGaN Superlattice Absorbption Layer, *IEEE Electron Device Letters*, Vol.30, No.3, March 2009
- [51] Takashi Matsuoka et al, Optical band gap energy of wurtzite InN, *Appl. Phys. Lett.* Vol.81 Number 7, 2002
- [52] Liu et al, Growth of In-rich and Ga-rich InGaN alloys by MOCVD and fabrication of InGaN-based photoelectrodes, *Phys. Status Solidi C* 7, No. 7–8, 1817– 1820 (2010) / DOI 10.1002/pssc.200983570
- [53] Pantha et al, Origin of background electron concentration in $\text{In}_x\text{Ga}_{1-x}\text{N}$ Alloys, *PHYSICAL REVIEW B* 84, 075327 (2011)
- [54] M. Horie et al, MOVPE growth and Mg doping of $\text{In}_x\text{Ga}_{1-x}\text{N}$ ($x\sim 0.4$) for solar cell, *Solar Energy Materials & Solar Cells* 93 (2009) 1013–1015

- [55] Young Huang et al, Growth and characterization of $\text{In}_x\text{Ga}_{1-x}\text{N}$ alloys by metalorganic chemical vapor deposition for solar cell applications, *Journal of Photonics for Energy* 028501-1 Vol. 2, 2012
- [56] V. Lebedev et al, Electron and Hole Accumulation in InN/InGaN heterostructures, *Phys. Status Solidi C* 8, No. 2, 485–487 (2011) / DOI 10.1002/pssc.201000441
- [57] J. Wu et al, Effects of electron concentration on the optical absorption edge of InN, *Appl. Phys. Lett.* 84, 2805 (2004); doi: 10.1063/1.1704853
- [58] Sunwoon Kim et al, Two-step growth of high quality GaN using V/III ratio variation in the initial growth stage, *Journal of Crystal Growth* 262 (2004) 7-13
- [59] Balakrishnam R. Jampana et al, Design and Realization of Wide-Band-Gap (2.67eV) InGaN p-n Junction Solar Cell, *IEEE electron Device Letters*, Vol.31, No.1, January 2010
- [60] Junxue Ran et al, Effects of doping on the crystalline quality and composition distribution in InGaN/GaN structures grown by MOCVD, *Journal of Crystal Growth* 298 (2007) 235-238
- [61] Xu Zhihao et al, Stress, structural and electrical properties of Si-doped GaN film grown by MOCVD, *Journal of Semiconductors* Vol.30, No.12 December 2009
- [62] J. M. Shah et al, Experimental analysis and theoretical model for anomalously high ideality factors ($n \approx 2.0$) in AlGaIn/GaN p-n junction diodes,” *J. Appl. Phys.*, vol. 94, no. 4, pp. 2627– 2630, Aug. 2003.
- [63] Jani et al, The Effect of Indium Composition on Open-Circuit Voltage of InGaIn Thin-Film Solar Cell: An Analytical and Computer Simulation Study, *AIP Conf. Proc.* 1451, 85 (2012); doi: 10.1063/1.4732375
- [64] Liwen Sang et al, Enhanced performance of InGaIn solar cell by using a super-thin AlN interlayer’ *APPLIED PHYSICS LETTERS* 99, 161109 (2011)
- [65] Xiao-Mei Cai et al, Dependence of the Property of InGaIn p-i-n Solar Cells on the Light Concentration and Temperature’ *IEEE TRANSACTIONS ON ELECTRON DEVICES*, VOL. 58, NO. 11, NOVEMBER 2011
- [66] <http://www.energyandcapital.com/articles/trickle-down-economics/1488>
- [67] <http://www.spec2000.net/09-xrd.htm>

- [68] K.S.A. Butcher et al, InN latest development and a review of the band-gap controversy, *Superlattices and Microstructures* 38 (2005) 1–37
- [69] Zhu Xue Liang et al, Characteristics of High In-content InGaN Alloys Grown by MOCVD, *Chin. Phys. Lett.*, Vol. 23, No.12 (2006) 3369
- [70] S.P. Fu et al, Effective mass of InN epilayers, *APL* Vol.85, No.9 (2004)
- [71] K.P. O'Donnell et al, Structural analysis of InGaN epilayers, *J. Phys.: Condens. Matter* 13 (2001) 6977–6991
- [72] Lei Wang et al, High barrier height GaN Schottky diodes: Pt/GaN and Pd/GaN, *Appl. Phys. Lett.* 68 (9), 26 February 1996
- [73] K.Mayes et al, High-power 280 nm AlGaIn light-emitting diodes based on an asymmetric single-quantum well, *APPLIED PHYSICS LETTERS* VOLUME 84, NUMBER 7 16 FEBRUARY 2004
- [74] Sebastian Schleussner et al, Effect of gallium grading in Cu(In,Ga)Se₂ solar-cell absorbers produced by multi-stage coevaporation, *Solar Energy Materials & Solar Cells* 95 (2011) 721–726
- [75] Qi Hua Fan et al, High efficiency silicon–germanium thin film solar cells using graded absorber layer, *Solar Energy Materials & Solar Cells* 94 (2010) 1300–1302
- [76] G.F. Brown et al, Finite element simulations of compositionally graded InGaIn solar cells, *Solar Energy Materials & Solar Cells* 94 (2010) 478–483